The composition of the deep continental crust inferred from geochemical and geophysical data

Laura G Sammon[1], William F mcdonough[1], and Walter D. Mooney[2]

[1]University of Maryland
[2]USGS Earthquake Science Center

November 26, 2022

Abstract

Combing geochemical and seismological results constrains the composition of the middle and lower continental crust better than either field can achieve alone. The inaccessible nature of the deep crust (typically >15 km) forces reliance on analogue samples and modeling results to interpret its bulk composition, evolution, and physical properties. A common practice relates major oxide compositions of small- to medium-scale samples (e.g. medium to high metamorphic grade terrains and xenoliths) to large scale measurements of seismic velocities (Vp, Vs, Vp/Vs) to determine the composition of the deep crust. We provide a framework for building crustal models with multidisciplinary constraints on composition. We present a global deep crustal model that documents compositional changes with depth and accounts for uncertainties in Moho depth, temperature, and physical and chemical properties. Our 3D deep crust global compositional model uses the USGS global seismic database (Mooney, 2015) and a compilation of geochemical analyses on amphibolite and granulite facies lithologies (Sammon McDonough, 2021). We find a compositional gradient from 61.2 ± 7.3 to 53.8 ± 3.0 wt.% SiO_2 from the middle to the base of the crust, with the equivalent lithological gradient ranging from quartz monzonite to gabbronorite. In addition, we calculate trace element abundances as a function of depth from their relationships to major oxides. From here, other lithospheric properties, such as Moho heat flux, are derived (18.8 ± 8.8 mW/m^2). This study provides a global assessment of major element composition in the deep continental crust.

The composition of the deep continental crust inferred from geochemical and geophysical data

Laura G. Sammon[1], William F. McDonough[1,2], Walter D. Mooney[3]

[1]Department of Geology, University of Maryland, College Park, MD 20742, USA
[2]Department of Earth Sciences and Research Center for Neutrino Science, Tohoku University, Sendai 980-8578, Japan
[3]Earthquake Science Center, United States Geological Survey, Menlo Park, CA 94025

Key Points:

- We present a global model for the composition of the deep continental crust constrained by geochemical and geophysical data
- Crustal SiO_2 content decreases with increasing depth, and compositions correlate to relative depth rather than absolute depth
- Moho heat flux is predicted at 18.8 ± 8.8 mW/m^2 for stable continent regions

Author ORCID numbers are

Laura G. Sammon : 0000-0002-4538-0700
William F. McDonough : 0000-0001-9154-3673
Walter D. Mooney : 0000-0002-5310-3631

Corresponding author: Laura G. Sammon, lsammon@umd.edu

Abstract

Combining geochemical and seismological models constrains the composition of the middle and lower continental crust better than either field can achieve alone. The inaccessible nature of the deep crust (typically >15 km) forces reliance on analogue samples and modeling results to interpret its bulk composition, evolution, and physical properties. A common practice relates major oxide compositions of small- to medium-scale samples (e.g. medium to high metamorphic grade terrains and xenoliths) to large scale measurements of seismic velocities (Vp, Vs, Vp/Vs) to determine the composition of the deep crust. We provide a framework for building crustal models with multidisciplinary constraints on composition. We present a global deep crustal model that documents compositional changes with depth and accounts for uncertainties in Moho depth, temperature, and physical and chemical properties. Our 3D deep crust global compositional model uses the USGS global seismic database (Mooney, 2015) and a compilation of geochemical analyses on amphibolite and granulite facies lithologies (Sammon & McDonough, 2021). We find a compositional gradient from 61.2 $\pm$ 7.3 to 53.8 $\pm$ 3.0 wt.% SiO2 from the middle to the base of the crust, with the equivalent lithological gradient ranging from quartz monzonite to gabbronorite. In addition, we calculate trace element abundances as a function of depth from their relationships to major oxides. From here, other lithospheric properties, such as Moho heat flux, are derived (18.8 $\pm$ 8.8 mW/m^2). This study provides a global assessment of major element composition in the deep continental crust.

Plain Language Summary

Using many different geophysical and geochemical techniques together helps us understand the composition of the bottom two-thirds of the continental crust. We cannot sample much of the continental crust directly because of how deep it is. Instead, we rely on rocks that have been brought to the surface and measurements of the speed of seismic waves traveling through the crust in order to determine what the deepest parts of the crust are made of. Accounting for various factors, such as crust temperature and tectonic setting, allows us to create a large-scale model for the composition of the deep crust.

1 Introduction

The deepest parts of Earth's crust are widely inaccessible to traditional geochemical sampling and so their composition is poorly understood. Only in areas where eruptions have brought xenoliths to the surface or where tectonic activity has exhumed medium and high grade metamorphic terrains are we able to *partially* determine the composition of the deep (middle and lower) continental crust. Even so, these *ex situ*, aged, weathered, and transported rocks may not adequately represent the overall, current composition of the deep crust. Such inaccessibility has challenged geochemists for decades, leading to competing models for continental crust and bulk silicate Earth (BSE) compositions, formation, and evolution. Dissonance in the geochemical community stems from known and unknown unknowns; that is, we are mostly certain of the uncertainties in our geochemical and petrological measurements, but we are uncertain if our samples are truly representative of large swathes of the deep crust or if they are merely point samples. Xenoliths and terrains are the sum of the processes that form them, which may cause them to differ from what is presently 15-45 km and deeper. The deep crust is an enigma, and compositions of xenoliths and high grade metamorphic terrains provide only an incomplete cipher.

Seismological techniques, however, provide another piece of the cipher by directly measuring the physical state of large sections of the deep crust. Physical properties (e.g. density, Poisson's ratio, Vp, and Vs) determined from these *in situ* geophysical experiments can be compared to laboratory experiments on rocks of known compositions, particularly medium to high grade metamorphic lithologies (amphibolite and granulite facies lithologies) to place constraints on estimates of deep crustal composition. Integrating geochemical and geophysical observations, related to each other by empirically (laboratory) derived thermodynamic properties, provides a reinforced, clearer, consistent picture of middle and lower crustal composition.

This study uses geophysical and geochemical datasets to build a global compositional model of the lower two-thirds of the continental crust. We generate a composition versus depth model for the middle and lower continental crust by applying thermodynamic modeling software to medium and high grade lithologies. We then compare the thermodynamically-generated seismic velocities to velocities obtained from seismological measurements to produce a jointly constrained geochemical-seismological compositional model.

2 Methods

Our model calculations are split into two main parts: 1) assembling data and performing thermodynamic calculations, and 2) adjusting model parameters to generate deep crustal compositional models with uncertainties. These calculations require seismic velocity depth profiles, Moho depths, and crustal temperature gradients for the areas of interest. Using the thermodynamic modeling software Perple_X, we calculate the probability that different deep crustal compositions could produce the observed seismic signal. These calculations are conducted using our modeling software, *CrustMaker*, which is provided as an electronic supplement. The calculation adopts a subdivision of the global continental crust into 13 tectonic regimes (Figures 1 and 2) to speed calculations and extrapolate results to areas with lower data coverage. The resolution of this global model is set to 1°latitude x 1°longitude x 3 km depth as a default, but can be changed in the model to suit user needs. We chose this default resolution for our global model based on the resolution of our crustal categories (each 1°x1° of crust was assigned a tectonic regime based on models such as CRUST1.0, Litho1.0, and modifications discussed further in Section 2.1), and the resolution of our crustal thickness and temperature data, the ramifications of which are discussed further in the Results section. For considering higher resolution, regional scale data, the same methods can be used. Instead of simplifying the crust into tectonic regimes, calculations are run for individual seismic velocity profiles, so that if there are, for example, 34 seismic velocity profiles as inputs, there will be 34 locations for which compositional profiles are generated.

We calculated the overlapping probability between measured seismic velocities and the Perple_X-derived velocities for amphibolites and granulites equilibrated at middle and lower crustal pressures and temperatures (assuming an average crustal density of 2900 ± 200 kg/m^3 (Wipperfurth et al. (2020), c.f. Christensen and Mooney (1995)). Integrating the area under both curves, the area shown as magenta in Figure 3, for a sample of composition X yields the total probability of sample X producing the observed seismic signal. Repeating this technique for a multitude of sample compositions at various depths and temperatures yields a final Monte Carlo model for deep crustal composition. Probability distributions are generated for Vp, Vs, and Vp/Vs and then multiplied together to constrain further the final probability.

2.1 Model Inputs

A global model of Vp, Vs, and Vp/Vs was generated from a compilation of over 8700 (Vp) and 1000 (Vs) 1-D seismic velocity profiles obtained from the Global Seismic Catalog (GSC) database (Mooney, 2015). Both controlled and passive source seismic velocity profiles were included to increase data coverage. We included only profiles with both Vp and Vs data that had been sampled at a minimum of 5 depth intervals within the crust. Figure 2 shows our tectonic regimes and the location of each seismic velocity profile used. We used global Moho depths from Litho1.0, except on the continental margins, where we reference Szwillus et al. (2019) Moho values. In comparison to Litho1.0, Szwillus et al. (2019) incorporated a larger dataset on the continental margins (∼1600 profiles) and did not average depths across the continent-ocean transition. Global Moho temperatures were generated from the TC15 global temperature model of Artemieva (2006). We assumed a linear temperature gradient within the continental crust, though we address the contributions from crustal heat production in a later section of this paper.

The foundation of the tectonic regimes chosen for this global model are the classifications of crust provided by the Crust family of models (Mooney et al., 1998). To further identify tectonic provinces and group together geophysically similar crust, we incorporated crustal thickness, seismic velocity (Vp, Vs), gravity anomaly, sediment thickness, crust elevation, and surface heat flux observations in a tSNE test (t-distributed stochastic neighbor embedding, perplexity of 50). Results generally favored grouping the continental crust into 8 - 12 regimes, mostly matching the designations already given in Crust1.0. We augmented these regimes with additional groupings, such as “Thinner Himalyan” crust, when it became clear that the seismic velocity structure of the perimeter of the Himalayas differed from the thickest Himalaya, the Tethyan region, and paleo-orogenies. Areas with sparse seismic coverage such as central South America, northern Africa, rely heavily on extrapolation of measurements from similar tectonic regimes. Average Vp and Vs profiles for most tectonic regimes were created from a distribution of tens to hundreds of individual measurements (Table 1). A notable exception is the “Continental Margins” regime, which was represented by an astounding $> 1{,}600$ profiles. Highly localized regimes, such as Andean or Himalayan crust, tended to have < 100 profiles due to the uniqueness of their crustal profiles.

Figure 1 and Table 1 show the proportion of different crustal regimes by surface area coverage. These tectonic provinces consider only crust exposed at the surface, so that regimes such as “Platform” have underlying crystalline crust that may be Proterozoic or Archean in age. The Proterozoic crust covers the largest fraction (32%) of the continental crust, followed by continental margins (16%).

A compilation of amphibolite and granulite facies major and trace element abundances (Sammon & McDonough, 2021) serves as our geochemical constraint on the deep (middle and lower) continental crust. We modeled amphibolite facies lithologies for the middle third of the crust and granulite facies lithologies for the bottom third, in agreement with the depth assignment of Rudnick and Gao (2014). We cannot confidently determine which portions of the deep crust are more appropriately represented by amphibolite versus granulite facies data with our current model. In theory, one metamorphic grade would have greater overall overlap with the seismic velocity profile(s), thus determining which is the more accurate rock type to use. In practice, however, amphibolite and granulite facies lithologies of the same SiO_2 abundance tend to have similar seismic velocities (see Section 3.1). As such, we have assumed that the metamorphic grade switches from amphibolite to granulite at 2/3 the crustal depth. Future studies should investigate using anisotropy in the deep crust to further establish lithology. Though trace elements do not participate in thermodynamic calculations, we were able to estimate trace element abundances based on a joint probability analysis with the mineral-forming major oxides. Samples were placed into bins based on the abundance of the oxide and trace element of interest (e.g. SiO_2 and U). Bin width was selected using Sturges rule ($N_{bins} = \log_2(N) + 1$). For each major oxide composition bin, there was then a correlated trace element abundance distribution.

2.2 Model Uncertainties

Errors in the seismic and geochemical inputs will skew results. It is imperative to understand the uncertainties in the input datasets if we want a clean picture of the uncertainty of our crustal composition models.

The program also will not assess the model error stemming from foundational assumptions about what types of lithologies should be used as geochemical inputs and the tectonic regimes assigned to global crust. These two assumptions are expected to control the systematic error of the model, which is why we made the program flexible and modular. Our approach facilitates testing different fundamental crustal models and highlights the projected differences in crust composition.

The primary sources of model error stem from uncertainty in the crustal temperature gradient and Moho depth. Again, these are parameters that can be set by the user. For our preferred model, the uncertainty on Moho depth is on the order of 10% or less in most areas of the global model. The temperature uncertainty is much greater. Global Moho temperatures are taken from Artemieva (2006), which reports no uncertainties. Therefore, uncertainty is taken as the standard deviation of all temperatures found within a given crustal regime (regimes discussed below), and the model runs a number of Monte Carlo iterations to produce a distribution of Moho depths and temperatures. Future results could be improved with Moho temperature models that quantify uncertainty more directly.

We have also attempted to mitigate the bias introduced by the oversampling of particular geochemical compositions. An oversampled composition, such as 100 input compositions with nearly identical major oxide content artificially inflates the probability of that composition in our final combined model. However, we do consider the reporting of compositions to be at least somewhat reflective of the proportion of rock types present in the deep crust, i.e. if the distribution of reported compositions is bimodal, the rocks in the deep crust are likely bimodal in composition. Therefore, we only considered a sample redundant if its oxide content differed from another's by < 3 wt.% (9 major oxides, using the distance between vectors formula $d = \sqrt{{x_1}^2 + {x_2}^2 + ... + {x_n}^2}$, where x_n is the difference in wt.% of an oxide between two samples), and its Perple_X generated values for Vp, Vs, and Vp/Vs were within uncertainty of each other.

The internal error contributed by calculational uncertainty is minimal. The overlap between of seismic velocity measurements and Perple_X-derived seismic velocities is calculated via trapezoidal numerical integration at intervals determined by the uncertainty in the seismological data. When the interval is too large to use for the integration, the program reduces the interval by half. The precision errors of Perple_X are generally negligible compared to the uncertainty on our other inputs (Connolly, 2005).

2.3 Quality, Expense, and Time: Global vs. Local Models

In numerical modeling, there is often a tradeoff between computation time and model resolution. For a global perspective of the continental crust, breadth and total model coverage may be more valuable than high data resolution, especially if results can be averaged over large areas. This large-scale, globe-encompassing model, however, comes with the choice of either short computation time and low resolution or longer computation time and higher resolution. Alternatively, those interested in a more in-depth analysis of a localized region may be able to accommodate higher resolution models. We suggest considering the following when determining whether to use a global or local scale model: data resolution (especially in seismic velocity profiles), data coverage, and model application. Those with data resolution on the scale of $> 0.5^\circ$ x 0.5° should consider using the global version of the script. Those with higher resolution, such as that provided by the Earthscope USArray, the AUSArray, or the J-ARRAY, should use the regional scale model. For the remainder of this study, we will analyze global model results. Sammon et al. (2020) presents an example of a local-scale composition analysis using a nascent version of this method.

3 Results

3.1 Emprical Composition-Velocity Trends

Seismic velocities correlate with SiO_2 content because of the high abundance of SiO_2 in granulite and amphibolite facies lithologies compared to all other oxides. Perple_X-calculated Vp and Vs values at given pressure-temperature conditions show a quadratic relationship between SiO_2 and velocity (Figures 4 and 5). The coefficients of the quadratic are determined for a given pressure and temperature, and are ultimately correlated to the empirical mineral physics datasets used in the Perple_X Gibbs free energy minimization. Amphibolite and granulite facies lithologies span similar Vp and Vs values, though the shapes of their distributions are marginally different. This is because their mineralogies are similar, both being dominated by plagioclase, garnet, and pyroxene, all of which have Vp of ~ 7 km/s and Vs of ~ 3.6 km/s. Despite considerable scatter in the Vs data, when paired with Vp, a clear trend emerges: increasing SiO_2 leads to decreasing velocities.

Higher Vp's correlate to lower silica content (Figures 6A and B). Higher Vp/Vs ratios also have decreased silica content, though for a given SiO_2 percentage, there is roughly a 10% spread in Vp/Vs. A slight curve in the amphibolite facies data becomes more pronounced in the granulites, developing an arcuate shape in the Vp/Vs vs. Vp plot. The same trends appear when analyzing Vp/Vs vs. Vs (Figures 6C and D), though the data is more acutely curved. For both amphibolite and granulite lithologies, increasing Vs can lead to either an increase or a decrease in Vp/Vs ratio. The maximum Vp/Vs for amphibolite facies lithologies at typical middle crustal P-T conditions, is expected at a Vs of about 3.5-3.8 km/s, a Vp of 6.5-7 km/s, and SiO_2 of 55 wt.%. For granulite, this maximum is expected at compositions closer to 60-63 wt.% SiO_2. Interestingly, the maximum Vp/Vs in granulite lithologies corresponds to the lowest Vs rather than the highest Vp, suggesting that Vs variations exert a stronger control on Vp/Vs ratios than does Vp.

3.2 Deep Crustal Density

We calculated deep crustal density by tracing the Vp and Vs values from Perple_X that overlapped with our seismological database back to their input samples. Then, instead of reporting the composition, we report the Perple_X-derived density of those input samples. We found that, similar to composition, deep crustal densities among the different tectonic provinces correlated much more closely when normalized to crustal thickness (Figure 7). The density uncertainty for each regime was 3%, a number that reflects the velocity uncertainties of our seismic velocity profiles. Deep crustal density ranges from 2700-2780 kg/m^3 at 13 km depth to 3290-3340 kg/m^3 at the Moho.

We note that, in order to calculate deep crustal pressure, and thus mineralogy and composition, we *already assumed* a bulk crustal density of 2900 kg/m^3. This initial assumption, though, does not greatly affect our composition results because there is, at most, a calculated pressure difference of <15% caused by using the 2900 kg/m^3 a-priori density vs. our model-generated density. This <15% pressure difference does not greatly change the stable mineral assemblages or velocities calculated by Perple_X for the deep crust.

3.3 Composition

Our main analysis focuses on SiO_2 abundance and its uncertainties because of its strong correlation to seismic velocities. The SiO_2 content at typical middle and lower crust depth intervals (Figure 8) is given in Table 2. All 9 major oxide inputs (SiO_2, TiO_2, Al_2O_3, CaO, MgO, FeO_T, MnO, K_2O, Na_2O) can be found in Table 3 and corresponding maps in Supplement Section 3. We use the notation "M_x", where x is the percent distance to the Moho (M) from the surface, to indicate depth on our figures so that tectonic regimes with varying crustal thicknesses are comparable. The deep crust starts at an intermediate composition, globally ranging from 58 - 68 wt.% SiO_2, and the bulk deep crust gradually transitions to 50-55 wt.% SiO_2 as it approaches the Moho (Figure 9). Global scale SiO_2 composition of the continental crust mostly decreases (or remains steadily mafic) with increasing depth for all tectonic regimes (Figure 10). Uncertainty in global SiO_2 also decreases with increasing depth due to fewer samples fitting the seismic signal in most cases. In the Andean and Himalayan tectonic regimes, however, the uncertainty tends to be larger than in other regions because of both the variation in geochemical data fitting the seismic signal and the relative sparsity of seismological profiles that sample the deepest parts of these thick tectonic regimes.

CaO content of the deep crust is also of interest due to its absolute abundance and significance as a contributor to sedimentary deposits, though only siliciclastic rocks and not carbonates were considered viable deep crust components (Wilkinson et al., 2009; Hartmann et al., 2012). In our model, Ca is mostly contained in plagioclases, pyroxenes, and garnets. CaO abundance tends to increase with depth because of the increasingly mafic nature of the deep crust, and therefore regions of low SiO_2 correlate with regions of high CaO. Globally, the median CaO at crustal depths of M_{85} is 9.1 $\pm$ 3.1 wt.% (Figure 11).

We can also derive the global distribution of a trace element if that trace element has a quantifiable relationship to one of the thermodynamic components (major oxides) used in our model. We used a geochemical database of samples with both major and trace element concentrations (Sammon & McDonough, 2021) to generate trace element maps as a function of major oxide abundance. We used a bivariate probability analysis to generate trace element distributions from a major oxide abundance, such as SiO_2, at a specific depth or location. Although we suggest using regional analyses for high resolution interpretations of trace element abundance, we present here global predictions and uncertainties for Sr (Figure 12) and U (Figure 13) content based on their relationships with CaO and SiO_2, respectively, as examples. Global average Sr increases with increasing CaO until plagioclase is no longer the dominant Ca-bearing mineral. Uncertainties on global U concentration span an order of magnitude because the abundance of U in a given metamorphic sample ranges from a few hundreds of ppb to a few ppm. U and SiO_2 abundances, however, are positively correlated, with median U increasing as median SiO_2 increases.

4 Discussion

4.1 SiO_2 and Overall Deep Crustal Composition

Figure 10 shows steady or decreasing SiO_2 with increasing depth. Figure 8 also makes it apparent, though, that the absolute SiO_2 at a given depth is not equal across different crustal types. For example, "Extended" crust appears mafic at 30 km depth while the "Thick Himalayan" crust is felsic at that depth, and "Proterozoic" crust falls in between (Figure 8). However, a more laterally consistent trend appears when comparing percent of the crustal column traversed rather than absolute depth (Figure 8). Most regions show a 5-10 wt.% decrease in median SiO_2 through the deep crust regardless of crustal thickness, so that SiO_2 decreases much faster in areas of thin crust than in areas of thick crust. We predict the global median SiO_2 at 50% above the Moho (or, alternatively, 50% crustal column thickness) to be 61.2 ± 7.3 wt.% SiO_2 with CIPW normative mineralogy of <10 wt.% alkali feldspar <15 wt.% quartz. The middle continental crust is therefore expected to resemble a quartz monzonite; the lower crust, with 53.8 ± 3.0 wt.% SiO_2 and 9.1 ± 3.1 wt.% CaO, is expected to transition to a gabbronorite.

Density sorting provides a simple mechanism for producing the compositional structure of the continental crust. The process of crustal genesis leaves mafic, restitic material at the base of the crust regardless of crustal thickness except in the few cases discussed in the next paragraph. More buoyant, felsic material ascends to the top of the crust, producing a gradient of SiO_2 that scales with crustal thickness. Without density sorting, the deep crust could be more mafic because it is simply closer to the mantle and therefore has a greater number of mafic intrusions. Our results do not indicate any need for sharp compositional boundaries in the deep crust. The $M_{X\%}$ notation reinforces the importance of scaled, relative depth in the crust rather than absolute depth for making compositional comparisons.

Two regions that appear conspicuously more felsic than the global deep crustal median are the Andes and the Thin Himalayan crust (Figure 10). A low temperature gradient could once again be the cause of this compositional difference, but we also must consider two other possibilities, particularly around the northern and northeastern Tibetan Plateau and Himalayan ramp. The first is that thick, convergent margins, especially in the Himalayas, might have layers of upper crustal material thrust deeper within the crust. In contrast, underthrust upper crustal material is less likely to appear in the Andes, which is a continent-ocean subduction zone. Alternatively, pockets of melt and partially melted material in the Andean middle and lower crust could reduce the shear wave velocity (Nelson et al., 1996; Regis et al., 2016; Searle et al., 2009; Caldwell et al., 2009; Schmitz et al., 1997; Schilling &

Partzsch, 2001). Because our current model does not factor in melt, slower Vs speeds would be attributed to a more felsic composition.

Other anomalous regions in Figure 8, particularly the continental margins of Antarctica, the East African rift zone, and the Sea of Japan, are likely caused by inaccurate temperature and Moho inputs. The East African Rift could appear felsic because the model's temperature gradient for that actively rifting region is too low; a cooler felsic composition can produce the same velocities as a warmer mafic composition. On the other hand, the highly localized, extremely felsic borders around Antarctica and between Japan and China likely indicate a misclassification of crust type and/or Moho depth. Thinner, oceanic crust has been documented in both regions (Hirata et al., 1992; Cho et al., 2004; Gohl, 2008; McCarthy et al., 2020). Better Moho and temperature resolution of the ocean-continent transition should increase the accuracy of compositional models in these regions.

Mafic granulite lithologies reach gravitational instability in the lower 10-20% of the average crustal column (Jagoutz et al., 2011), surpassing the upper mantle's density of 3300 kg/m^3. Therefore, according to Figure 7, most of the granulite facies lower crust for continental margins, Andean crust, Tethyan crust, and Phanerozoic crust should be gravitationally unstable. On the other hand, most other tectonic regimes would just reach mantle-like densities around the Moho depths. Thinner Himalayan type crust has a middle crustal density ∼9% lower than other regimes, correlating with negative seismic velocity anomalies. Arcs have the next lowest densities on average, suggesting that the denser lower crustal crustal beneath some arcs has already foundered (Jagoutz et al., 2011). The accreted arc of the "Andean" type crust in particular (pink triangles in Figure 7B) displays a stark decrease in density that has been associated with delamination of the lowermost crust (Kay & Kay, 1993; Ducea, 2011; Gao et al., 2021).

Forming continental crust via island arc processes, however, would then require the deep crust to become denser over time, since most of our crust regimes have lower crust calculated as denser than arcs. This can be achieved by cooling the crust, thickening it further, intra-crustal differentiation, or by mafic igneous injections into the lower crust. If our Moho temperature model is too hot, though, it will require denser, more mafic lower crust to explain the Vp and Vs values. As such, we note that the compositions discussed in the next section are intrinsically tied to Moho temperature, and may be skewed towards mafic granulites. Reducing the assumed crustal Moho temperatures would bring the estimated average crustal density closer to arc crust density.

There is a tradeoff between temperature and composition. Vp and Vs both carry a temperature dependence through their bulk and shear moduli, so accurate temperature estimates are imperative for modeling the crust; decreased seismic velocities can be the result of either higher temperature or greater SiO_2 content. The results presented here uses a linear temperature gradient through the crust from the TC15 global temperature model (Artemieva, 2006).

Table 4 reports one composition for the middle and one for the lower continental crust, a practice that is required to make meaningful comparisons to previous crustal models. While we recognize the assumption of a three-layer crust as an oversimplification of the diversity of crustal compositions, it is useful for some calculations to have average composition numbers for the crust; for instance, mantle tomography studies which require crustal correction, crustal corrections for geoneutrino studies; models of Earth's thermal history; and planetary scale compositional model for comparison with other rocky bodies. Compositional models in Table 4 have been normalized to 100 wt.%. Our middle crustal composition falls between two possible compositions given by Hacker et al. (2015): the fastest Vp endmember composition for the middle crust (62.7 wt.% SiO_2), and the middle crustal composition expected when the crust takes on a two compositional layer (upper and lower) structure, instead of three, (57.3 wt.% SiO_2). These SiO_2 estimates overlap with the 62 wt.% SiO_2 reported by Christensen and Mooney (1995) and fall on the mafic side of the uncertainty of the 63.5 wt.% SiO_2 middle crust reported by Rudnick and Nyblade (1999). Similar trends persist throughout the other major oxides. Our proposed lower crust composition is in close agreement with the lower crust of Rudnick and Gao (2014) and other mafic estimates (e.g. Hacker et al. (2015)'s fast Vp lower crust; Jagoutz and Schmidt (2012)). Models which predict a more intermediate-felsic lower crust, such as the North China craton lower crustal model of Liu et al. (2001) or the higher SiO_2, lower Vp options listed by Hacker et al. (2015), are not consistent with our global average, though isolated regions of more felsic lower crust may exist.

4.2 CaO and Sr

Bulk CaO concentration increases with depth (Figure 11) but as a component of mafic, siliciclastic rocks, not carbonate. This is due in part to our imposed amphibolite/granulite grade lithology restrictions on possible deep crust composition, but is reinforced by high density and Vp values observed in the deep crust. Carbonates, with deep crustal densities of approximately 2750 kg/m^3 and Vp's of 6.6 - 6.8 km/s (Christensen & Mooney, 1995), cannot substantially contribute to the deep crust. There are also few carbonate-dominated granulite facies xenoliths and terrains compared to the number of silicate granulites. A comparison of Figures 8B and 11 shows good correlation globally between regions of high SiO_2 and low CaO. Uncertainties in CaO track the same trends as SiO_2 as well, though the relative % uncertainty is roughly 10% higher on CaO than on SiO_2 because CaO does not follow velocity trends as cleanly as SiO_2.

CaO content does, however, predictably track with Sr concentration (Figures 11 and 12). Sr abundances cannot be directly derived from velocity calculations, but it can be predicted from its geochemical relationship with CaO. Patterns emerge when comparing the global distribution of Sr and CaO from two distinct sources: equilibrium mineralogy and data binning. First, Sr abundance increases for CaO contents between 2-6 wt.%, reaching a maximum at about 500 ppm Sr. However, Sr gradually decreases to 350 ppm as CaO increases to >6 wt.%. This shift in Sr abundance corresponds with the transition from plagioclase as the only Ca-bearing mineral phase to the addition of garnet and clinopyroxene as stable Ca-bearing phases.

Second, we see sharp jumps in Sr abundance in neighboring tectonic regions as a consequence of our data binning (Figure 12). The uncertainty on CaO content dictates that the compositional bin-widths are as wide as 2-3 wt.% for a total of six bins. Each bin has a central Sr value and distribution, leading to six possible median Sr abundances. The uncertainties on Sr are a combination of the systematic uncertainty (which CaO bin) and the statistical uncertainty (Sr variation within each bin) associated with each latitude by longitude voxel.

4.3 Heat Production and Moho Heat Flux

Low heat production is predicted for the bulk deep crust (~0.15 nW/kg or ~0.43 $\mu W/m^3$, assuming 2900 kg/m^3) (Fountain et al., 1987; Kukkonen et al., 1997; Jaupart et al., 2016). Areas with high predicted SiO_2, such as the Andes and continental margins, have estimated U content up to 4x higher than the global $M_{85\%}$ median (U = 0.173 ppm) because of the correlation between high SiO_2 samples and high U. Uncertainties on the global scale remain substantial and range by an order of magnitude. For this reason we recommend using regional heat producing element (HPE) data for understanding smaller scale variations and reserve this study's results for continent- or global-scale models. Using the methods discussed in the previous sections, we derived U abundance from SiO_2, and assume Th/U_{mass} of 3.77 ± 0.1 (Wipperfurth et al., 2018; Sammon & McDonough, 2021) at $M_{85\%}$ depth. Combining U and Th with K_2O abundance, we calculated an expected $M_{85\%}$ heat production of 0.056 nW/kg (0.19 $\mu W/m^3$, assuming 2900 kg/m^3). Figure 14 shows global heat production values, which are consistent with Huang et al. (2013); Rudnick and Gao (2014). Our model is also consistent with local studies based on HPE analyses of deep crustal xenoliths, such as Gruber et al. (2021); Pinet and Jaupart (1987); Ashwal et al. (1987). The uncertainties on this global model are dominated by uncertainties on

U abundances. Even so, our *uncertainty on the median or central value* of HPEs or heat production is well constrained at ± 0.1%. While possible heat production values span an order of magnitude, the median/average heat production value is better constrained.

Given density, composition, surface heat flux (Lucazeau, 2019; Shen et al., 2020) parameters (Table 5), and an average thermal conductivity for crustal rocks (i.e., 2.65 W/m/K; Miao et al., 2014), we can generate a model prediction for the global Moho heat flux:

$$Q_M = Q_0 - (H_{crustal} * z_{crustal})$$

where Q_0 is surface heat flux (W/m^2), $H_{crustal}$ is crustal heat production (W/m^3), $z_{crustal}$ is the crustal thickness (m), and Q_M is Moho heat flux (W/m^2), with only vertical variations in heat flux being considered. Figure 15 shows the expected Moho heat flux based on our deep crustal model and a Gaschnig et al. (2016) model for the upper crust composition.

The median global continental Moho heat flux, shown in Figure 15, is 24.8 ± 11.9 mW/m^3. However, if we consider only tectonically stable regions, the median Moho heat flux is 18.8 ± 8.8 mW/m^3, though, both values overlap with stable continent estimates (Jaupart et al., 2007). The Moho heat flux calculations depends substantially on the assumed HPE abundance model for the upper crust, as it contributes ∼60 % of the total crustal heat production in most regions. The middle crust, while not as HPE enriched as the upper crust, still produces about 30% of crustal heat production. The mafic lower crust produces <10%. Pairing an upper crustal composition of Gaschnig et al. (2016) with our deep crustal composition yields a reasonable Moho heat flux for tectonically stable regions and agrees with the prediction by Jaupart et al. (2007), but marginally so for models having on average a slow Vp crust structure (Hacker et al., 2015). Using these upper crustal U and Th abundances in low heat flux areas, though, particularly cratonic regions, results in roughly 6% (by area) of the continents having a negative heat flux across the Moho (an unreasonable condition) – or more likely, other factors, such as heat dissipation through fluid circulation in the near surface, are needed to explain these low surface heat flux regions (e.g., 20-40 mW/m^2). Alternatively, the assumed upper crustal heat production values may need to be lowered, however, before making such adjustments further research is required. Most of these low heat flux areas coincide with stable cratonic lithosphere, where low heat flux and heat production is not a new observation (e.g., Nyblade and Pollack (1993); Kukkonen et al. (1997); Jaupart et al. (2007); Cammarano and Guerri (2017)). Various studies estimate cratonic crustal heat production to be between 0.6 and 1 μW/m^3 (Gruber et al., 2021; Jaupart et al., 2016; Phaneuf & Mareschal, 2014; Mareschal & Jaupart, 2013; Jaupart et al., 2014), so we approximate upper crustal heat production as 0.8 μW/m^3, which is the maximum permissible heat production value found by Rudnick and Nyblade (1999) for the Kalahari craton and the maximum average crustal heat production expected for crust $\geqslant$2 Ga (Jaupart et al., 2016).

5 Conclusions

We have constructed a global model for the deep continental crust composition by synthesizing seismic, temperature, heat flux, and geochemical data. We predict deep crustal compositions on the global scale using major and trace element compositions from amphibolite and granulite facies lithologies, and seismic velocity profiles. Our proposed global compositional model uses a USGS database of crustal seismic studies, published compositions for thousands of medium and high grade metamorphic rocks, and constraints on Moho depth (Pasyanos et al., 2014; Szwillus et al., 2019), crust temperature (Artemieva, 2006), and surface heat flux (Lucazeau, 2019; Shen et al., 2020).

Vp, Vs, and Vp/Vs correlate well with bulk rock SiO_2 content because of its high abundance in rocks, and SiO_2 can be used as a predictor of velocity if temperature can be estimated accurately. Globally, SiO_2 concentration tends to decrease with increasing depth, leading to a predominantly mafic and intermediate-mafic base of the crust. The decreased density and less mafic nature of the lower crust in younger and tectonically active crust, such as arcs and active mountain ranges, suggests that they are hotter than our temperature model predicts, that they have undergone lower crustal delamination, or both. Global median SiO_2 content for the middle and lower crust are 61.2 ± 7.31 and 50.1 ± 3.48 wt.%, respectively, though steady composition and velocity gradients in the deep crust urge us to embrace a less distinctly layered view of the crust. This mid-to-deep crustal gradient in wt.% SiO_2 is the equivalent of a lithological gradient ranging from quartz monzonite to gabbronorite. We predict the abundances of multiple thermodynamic oxides, many of which are correlated to trace element abundances. This correlation allows us to derive expected heat production in the deep crust. We therefore also predict a Moho heat flux of 18.8 ± 8.8 mW/m^2 for tectonically stable regions.

6 Author Contributions

LGS, WFM and WDM contributed to the conceptualization and methodological development of this project. LGS did software development, modeling, visualization, and writing. WFM and WDM contributed input and discussion throughout, as well as with the revising and editing. WDM contributed the compilation of seismic surveys used to build this model. All authors have read and approved this manuscript.

Acknowledgments

We gratefully acknowledge the support by NSF grants EAR1650365 and 2050374 to WFM and support from the United States Geological Survey Earthquake Hazards Program to WDM. We also thank Wolfgang Szwillus for his insights on heat flow modeling. Data and modeling software can be found at https://doi.org/10.5281/zenodo.5087347.

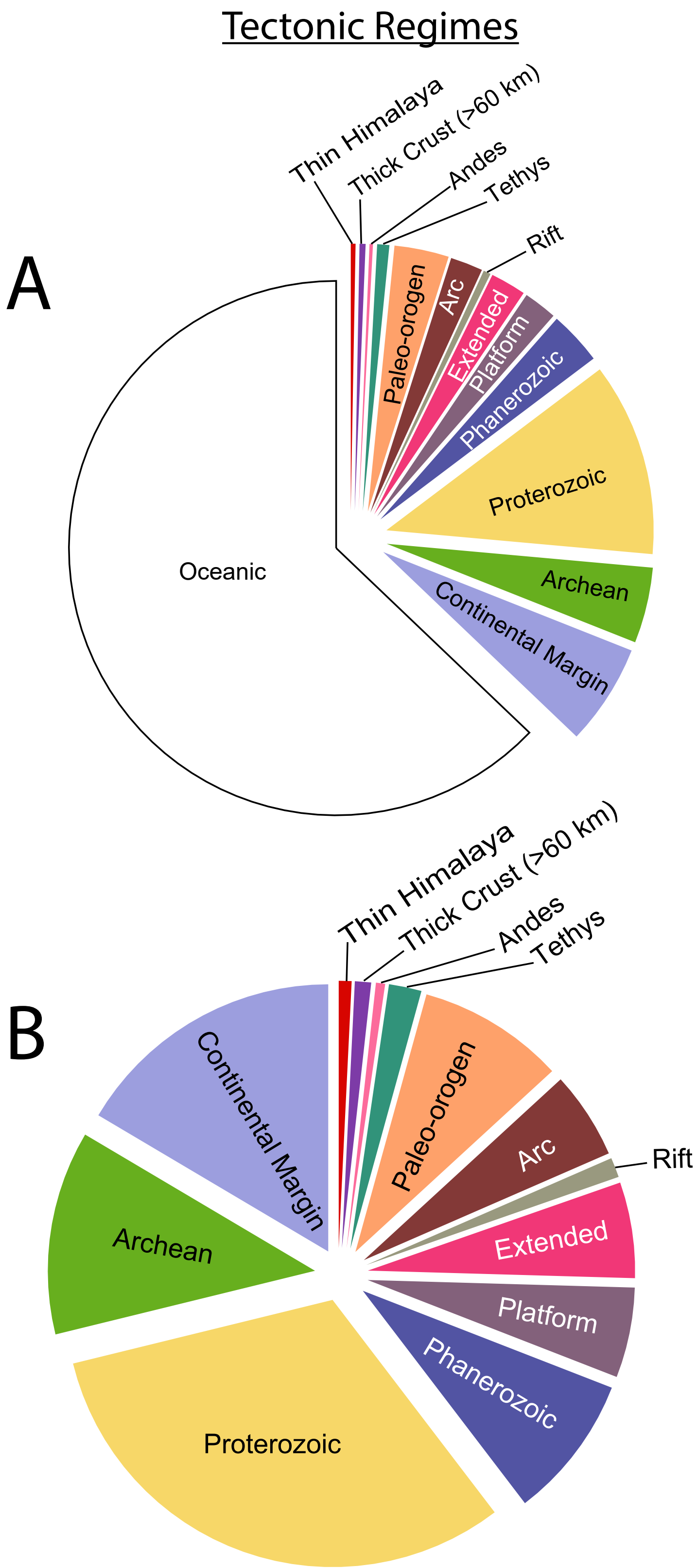

Figure 1: The weighted area proportion of crustal types, or “tectonic regimes”, used for our model as A) a fraction of total crust and B) a fraction of continental crust. Proterozoic crust is most abundant (32% of the continental crust), followed by continental margins (16%) and Archean crust (12%). Modern and paleo-orogens, including arcs, make up a combined 19% of the continental crust in our model.

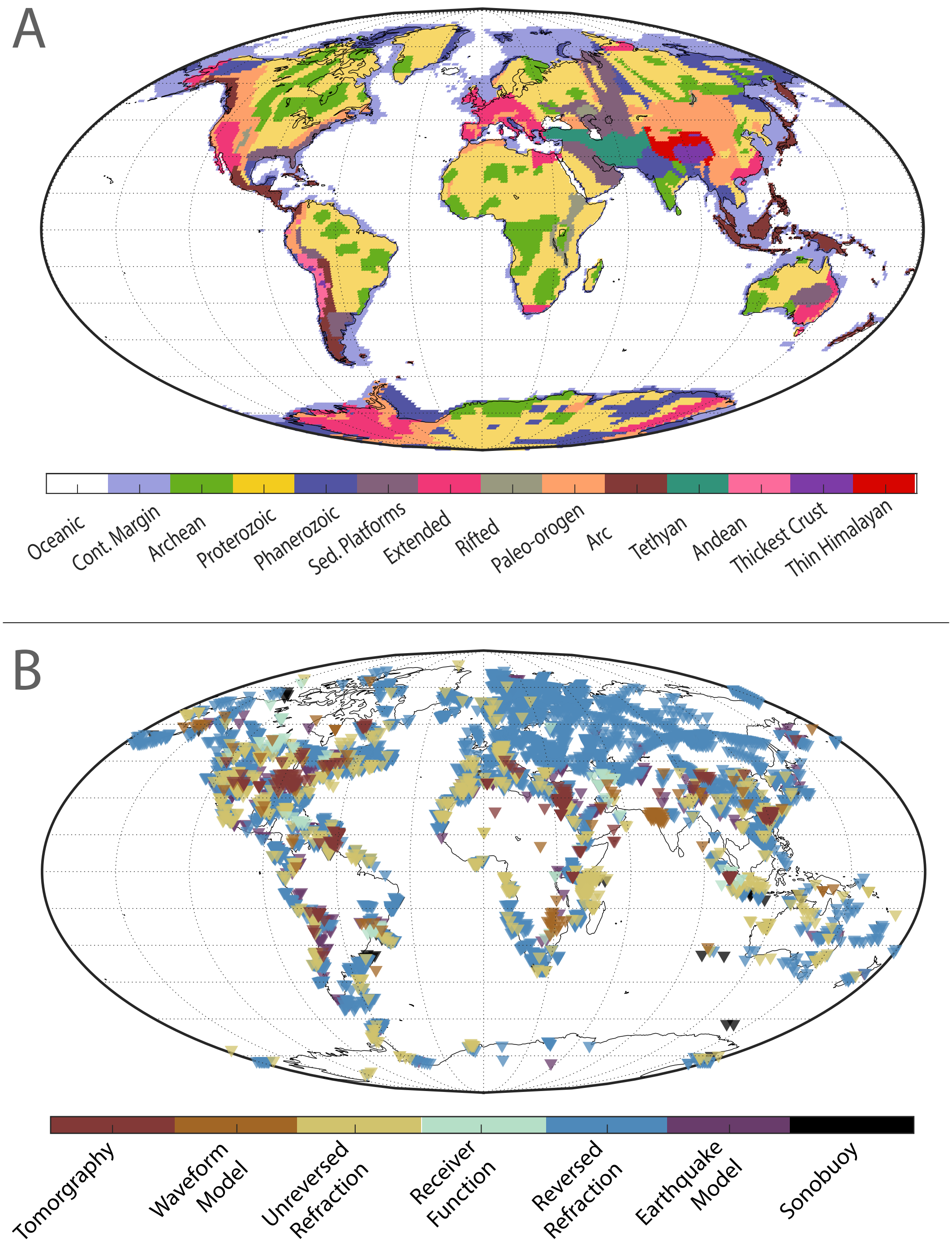

Figure 2: A) The mapped distribution of our 13 crust types and B) the seismic velocity profile data distribution from the USGS database. Data coverage is greatest in the northern hemisphere while places with less coverage, like Africa and Antarctica, rely more heavily on extrapolation of crust type.

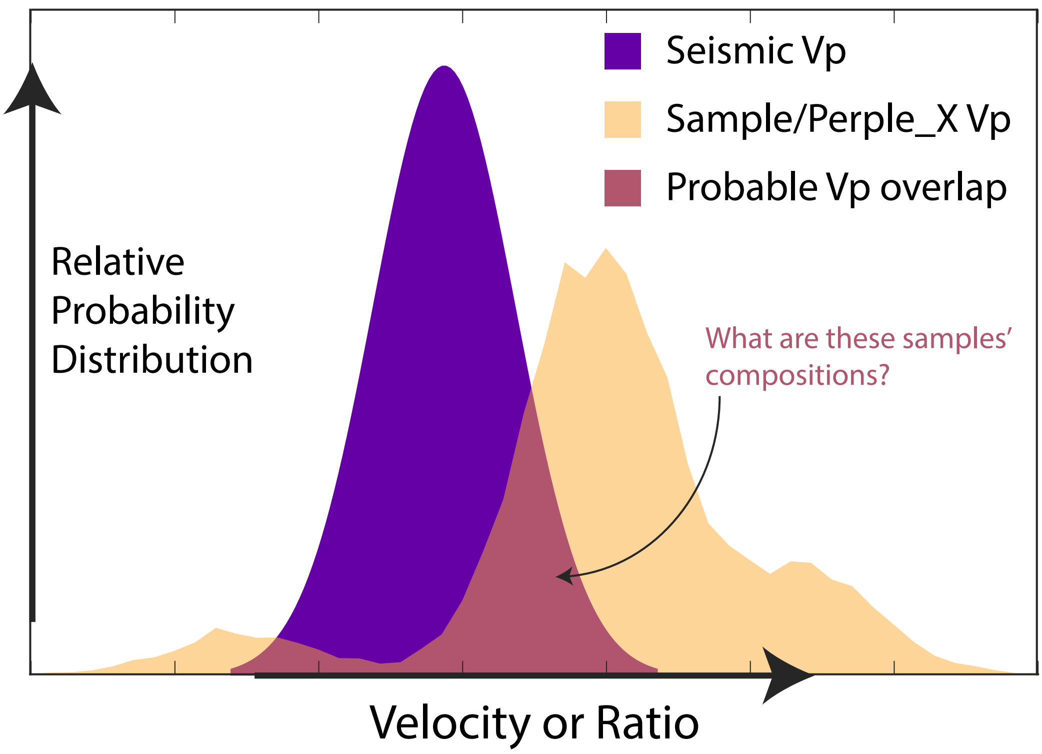

Figure 3: A conceptual illustration of overlapping velocity distributions used to identify probable crust compositions. The central pink region of the diagram, where the measured seismic velocity distribution (purple) overlaps the Perple_X-generated velocity distribution (tan), are the velocities that are considered the best-fit by the model. The model records the compositions of the samples that can produce the best-fit velocities.

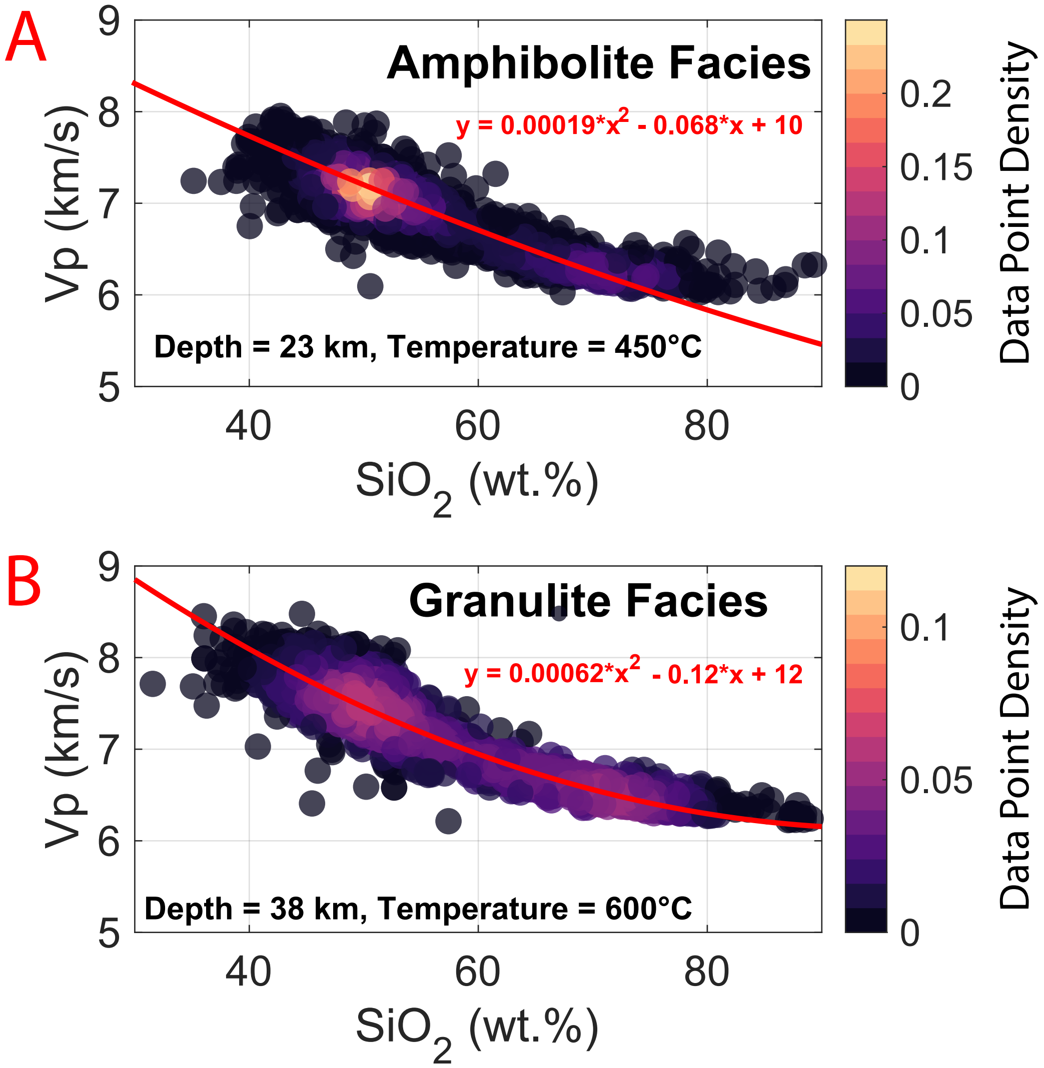

Figure 4: Vp as a function of SiO_2 wt.% for amphibolite (A) and granulite (B) facies lithologies at expected deep crustal pressures and temperatures. The color of the data points indicates percent data point density, with the brighter colors indicating more data points. The red line shows the best fit quadratic regression between Vp and SiO_2 and changes for different temperatures and pressures.

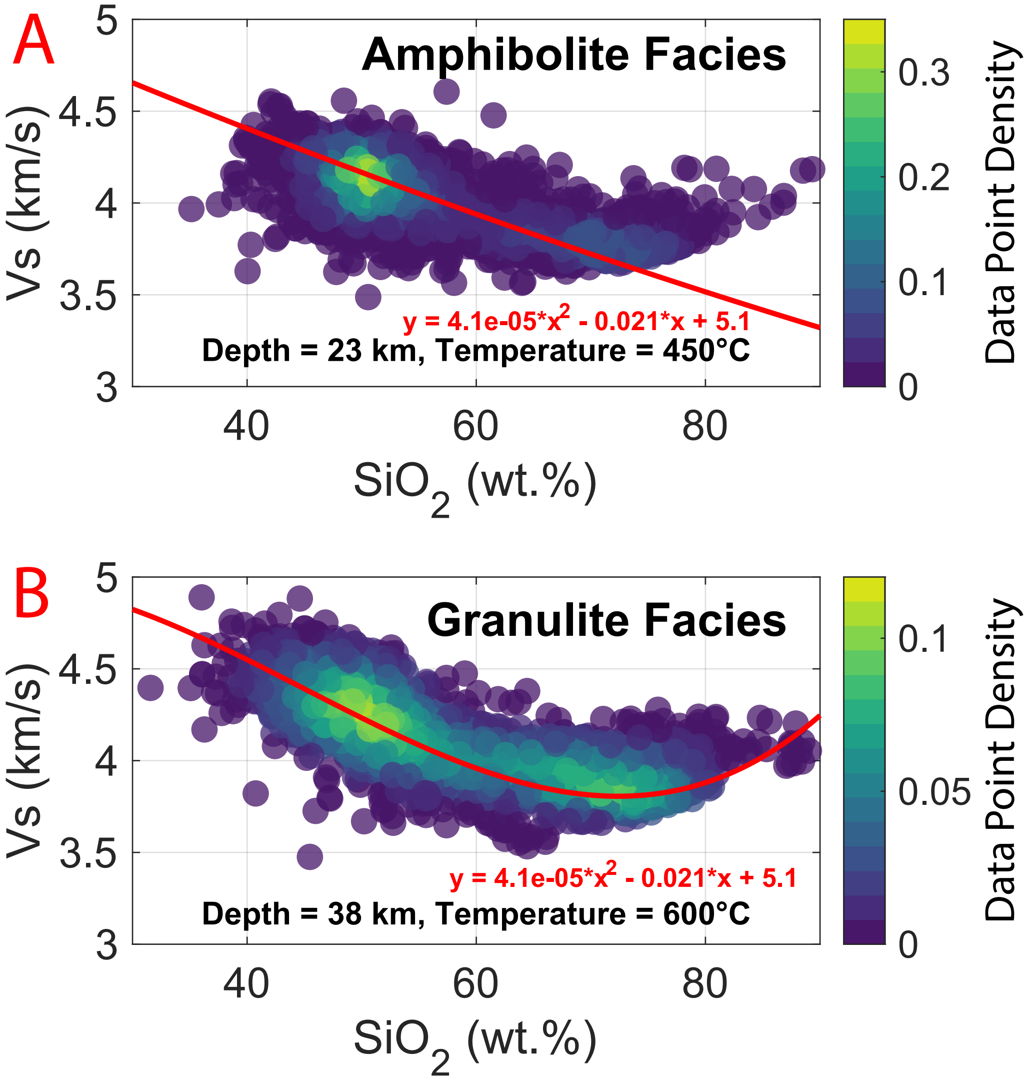

Figure 5: Vs as a function of SiO_2 wt.% for amphibolite (A) and granulite (B) facies litholoiges at expected deep crustal pressures and temperatures, generated through Perple_X. The color of the data points indicates percent data point density, with the brighter colors indicating more data points. The red line shows the best fit quadratic regression between Vs and SiO_2 and changes for different temperatures and pressures. There is more scatter between SiO_2 and Vs than SiO_2 and Vp, but can be combined for a tighter constraint on composition than either compressional or shear velocity alone.

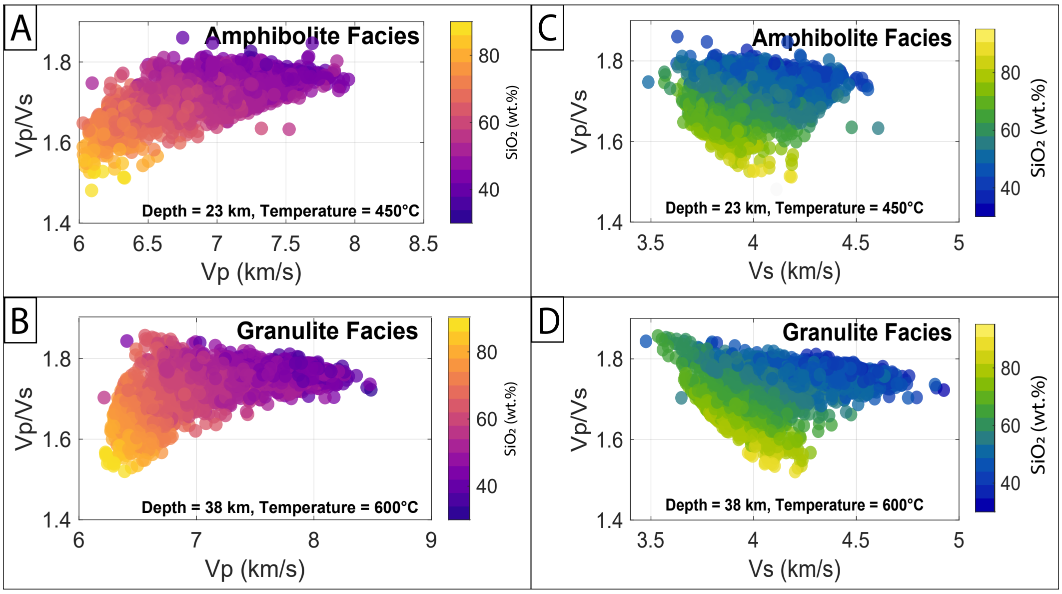

Figure 6: Vp/Vs plotted against (A) Vp and (B) Vs for amphibolite facies lithologies, and (C) Vp and (D) Vs for granulite facies lithologies at deep crustal temperatures and pressures generated through Perple_X. Color indicates SiO_2 concentration. Low Vp's correlate to a low Vp/Vs ratio.

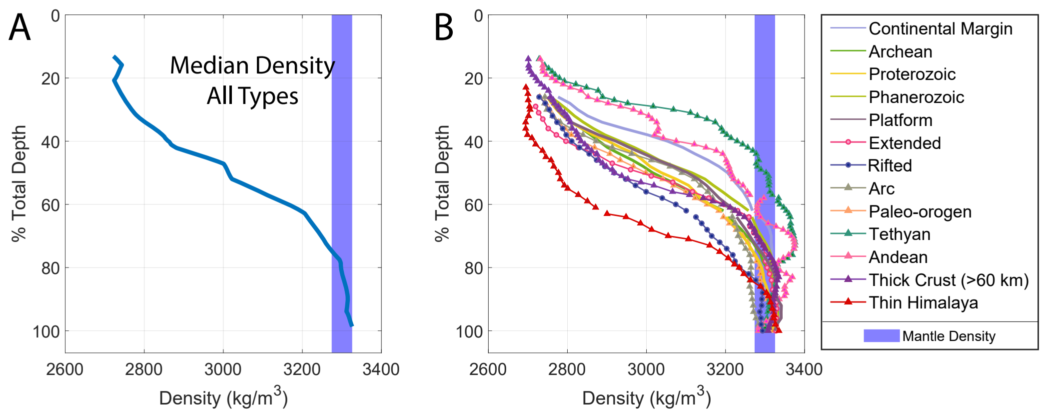

Figure 7: Calculated density normalized to depth for (A) average continental crust and (B) our different tectonic regimes with an imposed lithology transition (amphibolite to granulite facies) at 2/3 total crust depth. By this method, the bottom $\sim 20-30\%$

of the crust approaches or exceeds mantle density.

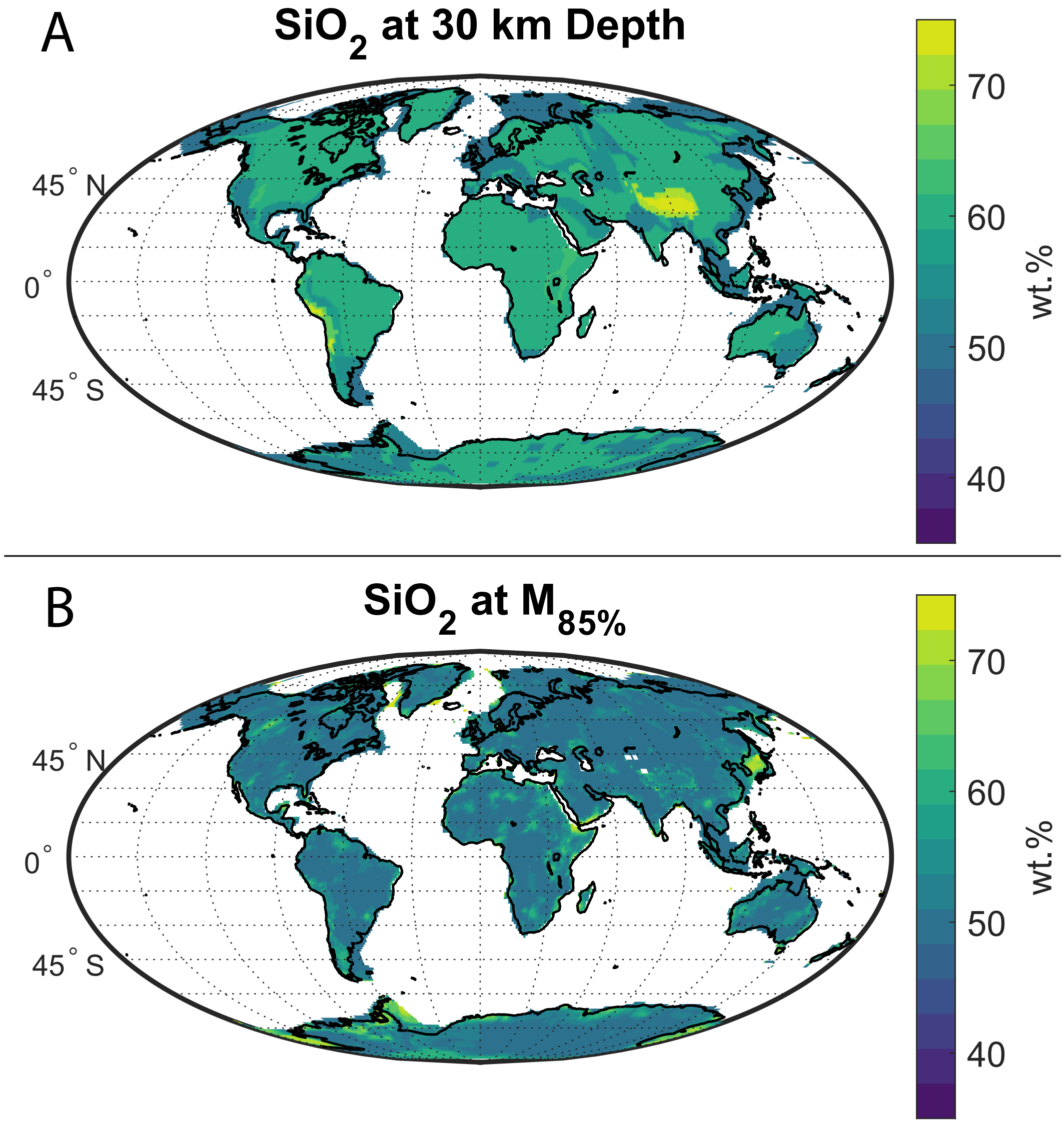

Figure 8: Global SiO_2 composition at a depth of 30 km shows regional distinctions whereas measuring composition at a crustal depth relative to the Moho ($M_{85\%}$ notation = 85% of the total crustal depth) produces a view of a deep crust that is contiguous and decreases in SiO_2 gradually with depth. Areas of high projected SiO_2 include the Himalayas, Andes, East African rift, and some continental margins. While the Himalayas and Andes may show compositional features, the high SiO_2 in some rifts and continental margins are likely from model input inaccuracies

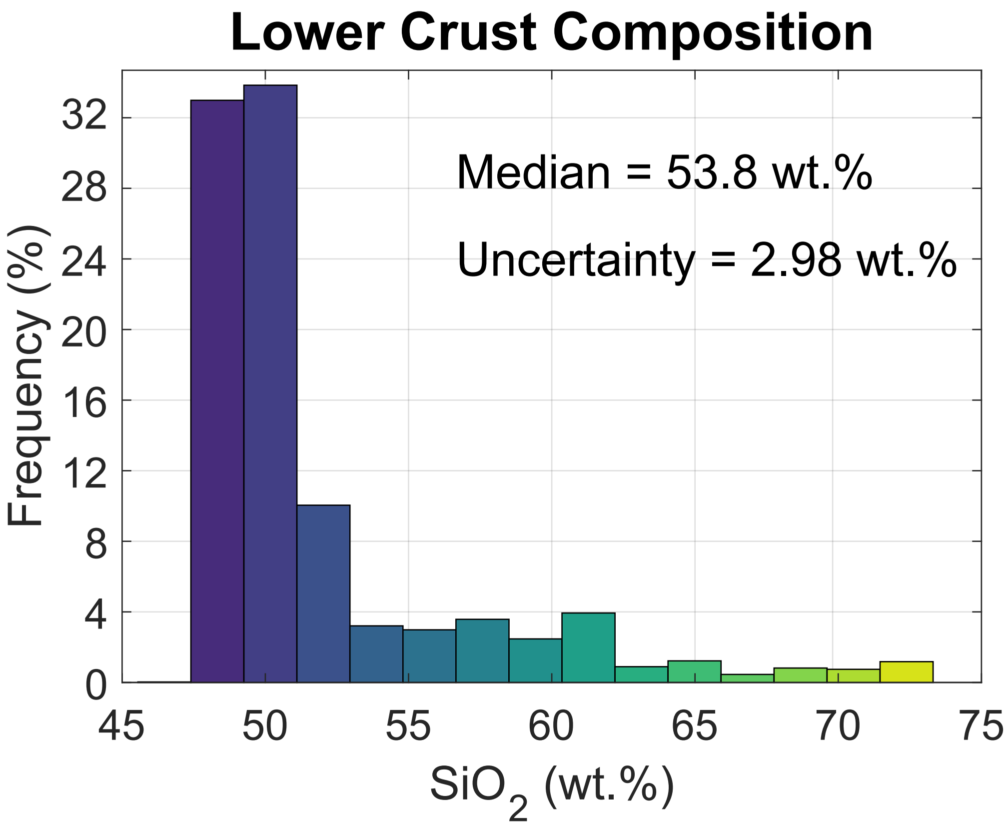

Figure 9: The area weighted distribution of SiO_2 shows that global lower crust (bottom 1/3 of crust) favors values around 50 wt.% while possibly reaching as high as 70 wt.% in limited areas. The median lower crustal SiO_2 is 53.8 $\pm$ 2.98 wt.%, though the distribution is far from normal.

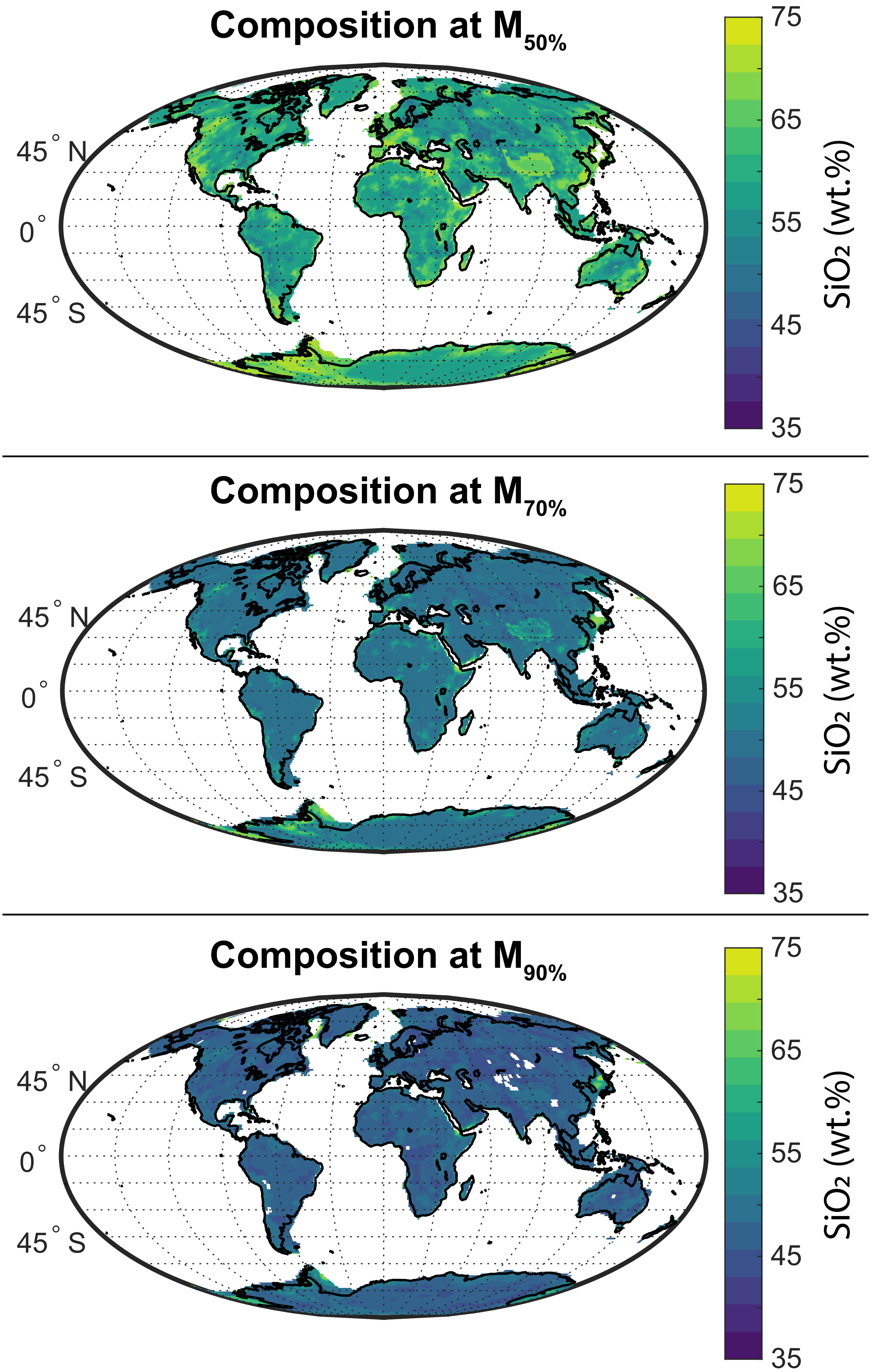

Figure 10: Global SiO_2 decreases with increasing depth from the middle to the bottom of the continental crust. The middle crust $M_{50\%}$ ranges from 60 to 65 wt.% SiO_2 in most areas and increases at a rate of about wt.% per km until reaching the base of the crust. Uncertainties can be found in Supplemental Figure SXXX[].

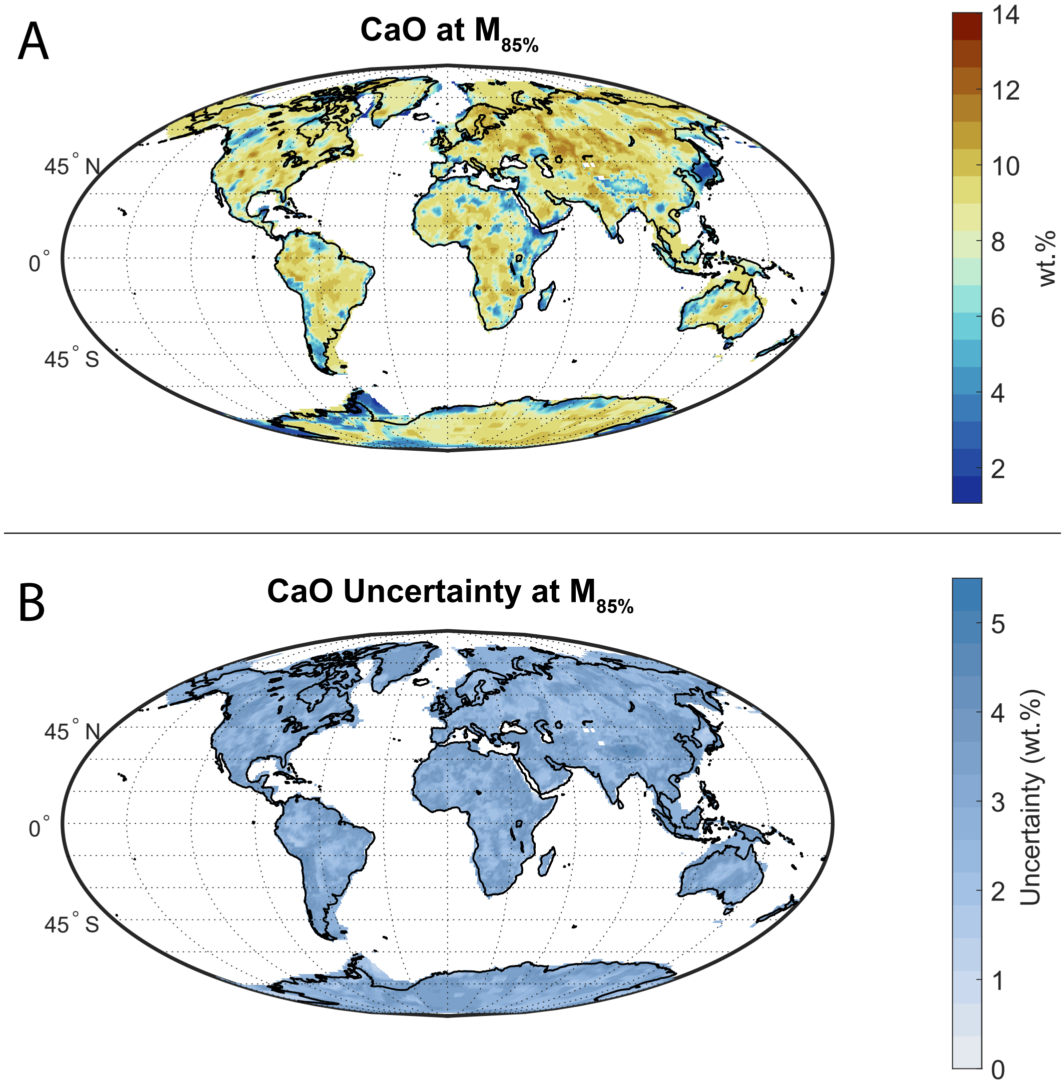

Figure 11: Global CaO abundance and uncertainty at 85% of the total crustal depth. Areas of low CaO correlate to areas of high SiO_2. There does not appear to be any correlation between CaO content and uncertainty, with most regions having 3 to 4 wt.% uncertainty regardless of CaO abundance.

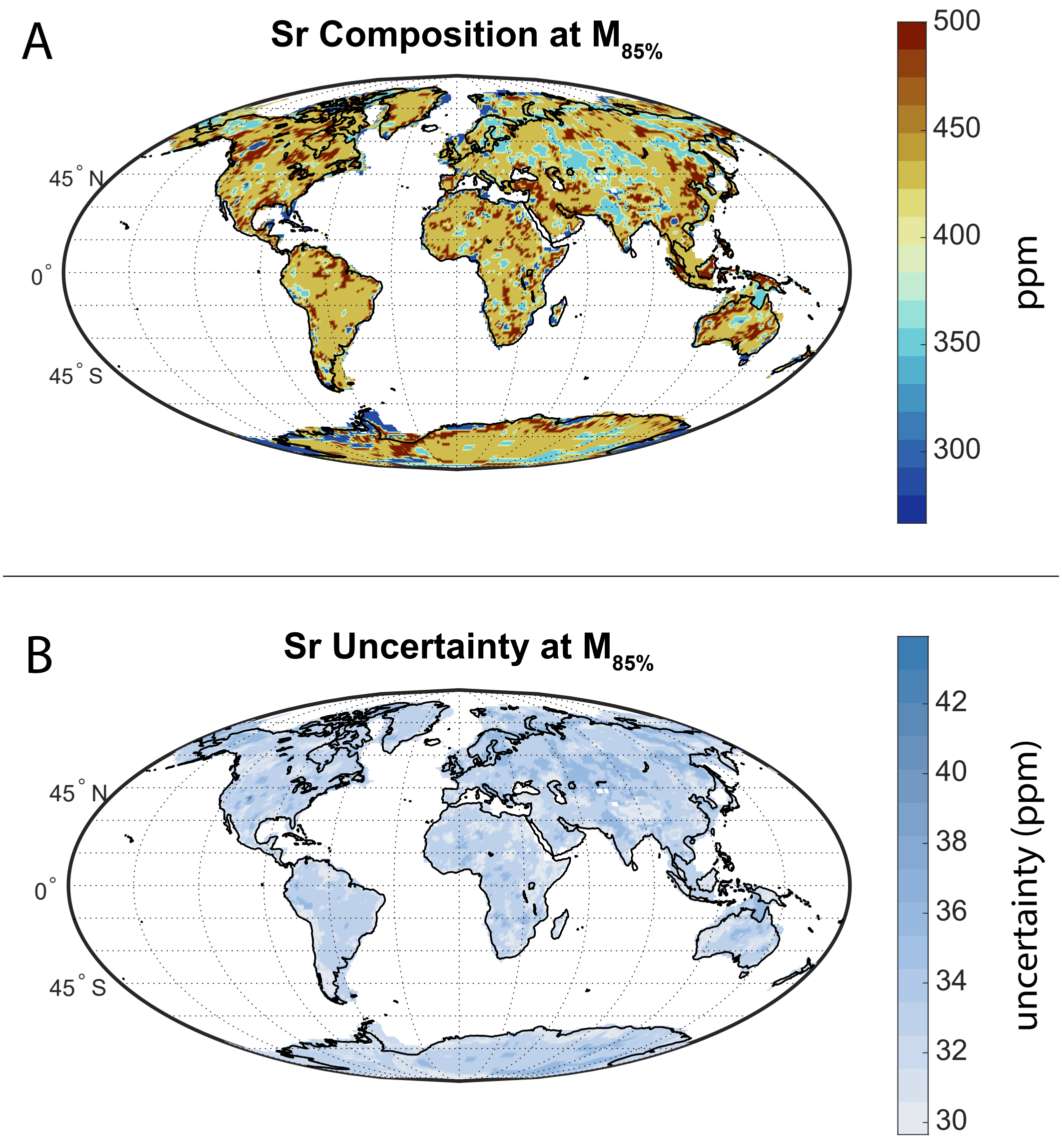

Figure 12: Global Sr abundance and uncertainty was derived from a joint probability analysis with CaO at 85% of the total crustal depth. Average global Sr abundance is ± ppm.

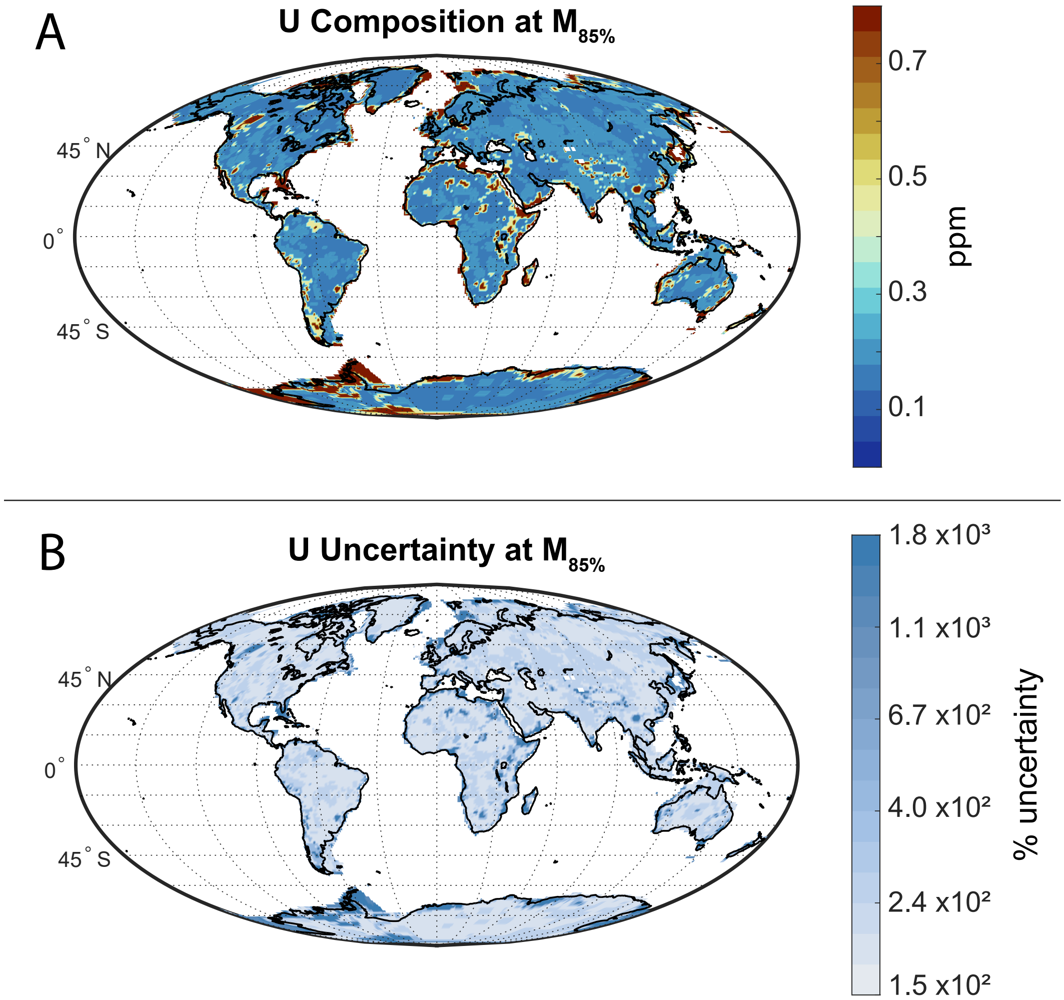

Figure 13: Global U abundance derived from a joint probability analysis with SiO_2 at 85% of the total crustal depth. Uncertainties span orders of magnitude because of the range of possible U values, but the global median at this depth is ∼0.2 ppm U. Regions of high SiO_2, especially the potentially inaccurate continental margin of Antarctica correlate with high U and the highest uncertainties.

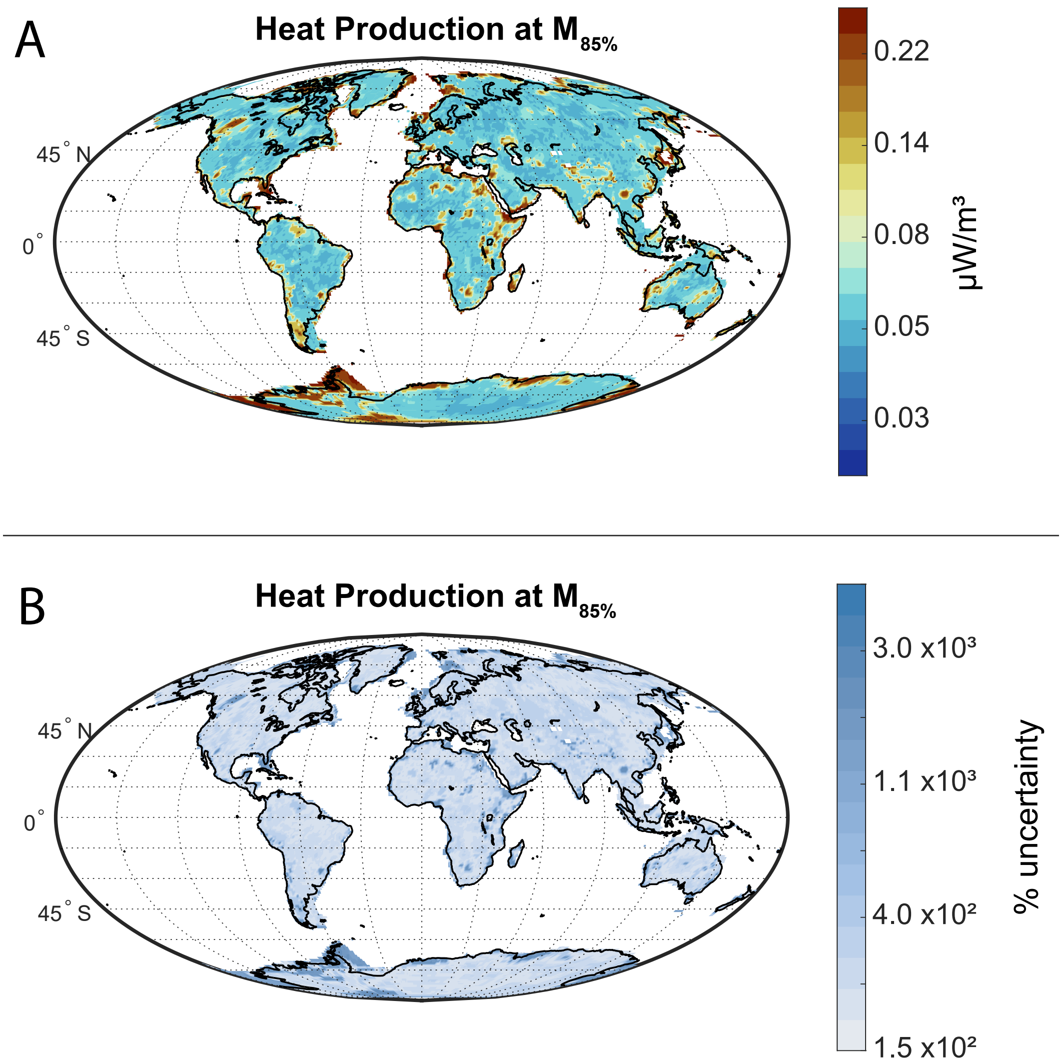

Figure 14: Global heat production at the $M_{85\%}$ layer. The K_2O abundances were directly calculated from Perple_X, whereas U and Th abundances were derived from relationships to SiO_2 and a Th/U mass ratio of 3.7 ± 0.1. Uncertainties in U abundances dominate the overall uncertainty (see Figure 13).

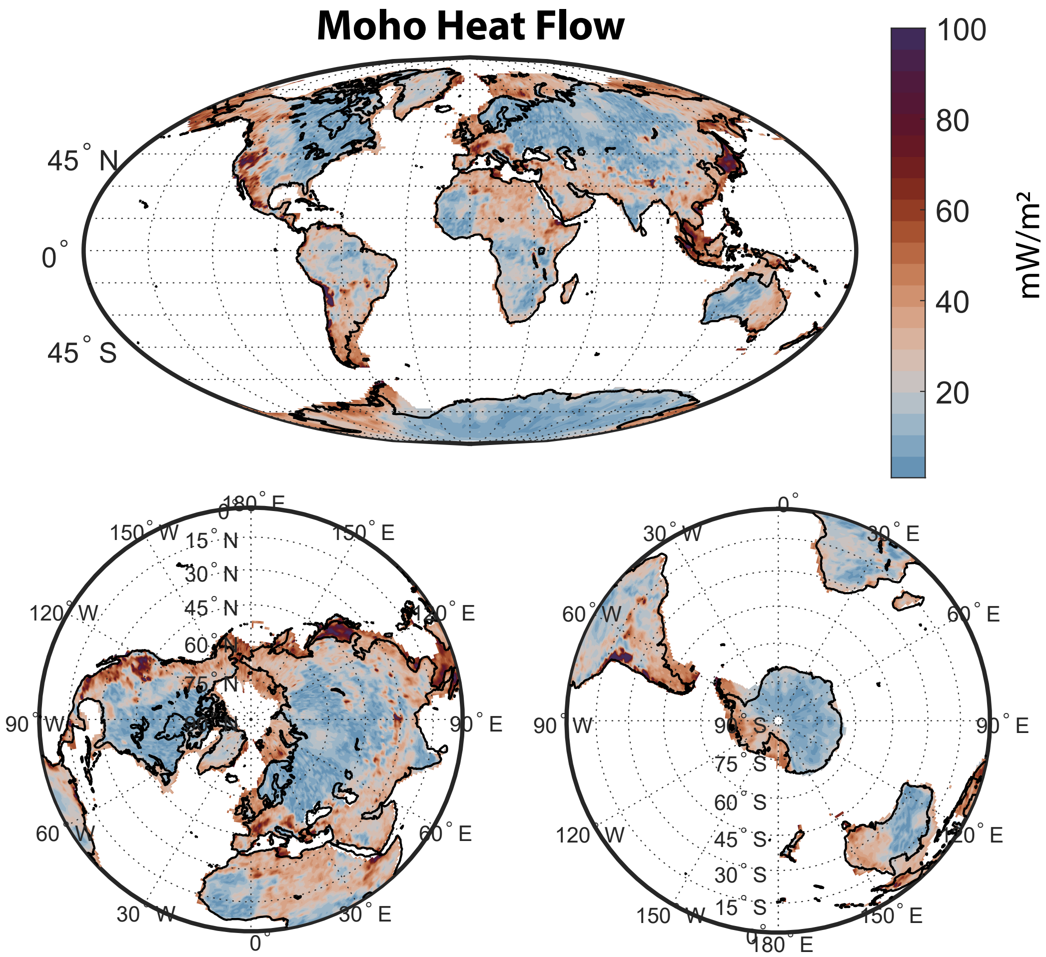

Figure 15: Global heat flux across the Moho calculated by subtracting crustal heat production from measurements of surface heat flux. The median subcontinental Moho heat flux is 24.8 ± 11.9 mW/m^2 globally and 18.8 ± 8.8 mW/m^2 for stable continent. This result assumes a uniform upper crustal heat production of 0.8 μW/m^3 for cratonic and 1.65 μW/m^3 for non-cratonic regions.

Table 1: Crustal Regimes by Surface Area

Crustal Regime	% All Crust	% Continental Crust	Number of Profiles
Oceanic	63	-	-
Continental Margin	6	16	1693
Archean	5	12	416
Proterozoic	12	32	919
Phanerozoic	3	9	353
Platform	2	5	318
Extended	2	6	403
Rifted	<1	1	148
Arc	2	5	262
Paleo-orogenic	3	9	565
Tethyan	<1	2	59
Andean	<1	1	31
Thick Crust	<1	1	106
Thin Himalayan	<1	1	28

Table 2: Median SiO_2 in wt.% for different tectonic regimes

	SiO_2 at $M_{50\%}$ ($\sim$ *middle crust*)	Uncertainty $\pm$	SiO_2 at $M_{85\%}$ ($\sim$ *lower crust*)	Uncertainty $\pm$
Continental Margin	61.1	10.2	52.8	2.7
Archean	61.0	7.8	51.9	2.9
Proterozoic	62.0	7.3	52.9	3.7
Phanerozoic	61.5	9.2	51.8	2.5
Platform	58.9	7.6	51.8	2.7
Extended	68.9	7.6	52.7	2.4
Rifted	66.8	7.3	57.8	6.5
Arc	68.7	9.8	57.6	6.9
Paleo-orogenic	63.9	9.2	52.7	3.4
Tethyan	63.9	9.4	52.3	3.1
Andean	59.9	9.1	56.0	6.9
Thick Crust	68.2	8.8	58.4	8.6
Thin Himalayan	70.7	5.9	51.3	2.2

Table 3: Middle and Lower Crust Bulk Composition in wt.%

	Composition at $M_{50\%}$ ($\sim$ *middle crust*)	Uncertainty $\pm$	Composition at $M_{85\%}$ ($\sim$ *lower crust*)	Uncertainty $\pm$
SiO_2	61.2	7.31	53.8	2.98
TiO_2	0.77	0.38	0.87	0.40
Al_2O_3	16.4	1.68	17.3	3.46
FeO	7.52	2.93	9.75	2.25
MnO	0.12	0.06	0.17	0.06
MgO	3.04	1.73	5.92	2.81
CaO	5.72	2.05	9.07	3.08
Na_2O	3.77	0.81	2.28	1.02
K_2O	1.46	0.97	0.81	0.96

Table 4: Continental crust composition estimates

	Christen & Mooney, 1995	Liu et al., 2001	Jagoutz & Schmidt, 2012	Rudnick & Gao, 2014	Hacker et al., 2015†	Hacker et al., 2015‡	This Study
	Middle Crust						
SiO_2	62	-	-	63.5	62.7	57.3	61.2
TiO_2	-	-	-	0.69	0.8	0.99	0.77
Al_2O_3	-	-	-	15	15.7	16.8	16.4
FeO_T	-	-	-	6.02	6.76	8.15	7.52
MnO	-	-	-	0.10	0.13	0.16	0.12
MgO	-	-	-	3.59	3.51	4.46	3.04
CaO	-	-	-	5.25	5.27	6.63	5.72
Na_2O	-	-	-	3.39	3.42	3.89	3.77
K_2O	-	-	-	2.3	1.6	1.42	1.46
Mg#	-	-	-	51.5	48.1	43.4	41.9
	Lower Crust						
SiO_2	47	58.3	52.16	53.4	50.7	57.3	53.8
TiO_2	-	0.59	0.78	0.82	1.24	0.99	0.87
Al_2O_3	-	13.6	18.68	16.9	16.5	16.8	16.3
FeO_T	-	5.32	8.41	8.57	10.39	8.15	9.75
MnO	-	0.08	0.17	0.10	0.19	0.16	0.17
MgO	-	9.58	5.86	7.24	7.03	4.46	5.92
CaO	-	4.54	10.79	9.59	10.1	6.63	9.07
Na_2O	-	2.54	2.56	2.65	2.8	3.89	2.28
K_2O	-	3.23	0.41	0.61	0.79	1.42	0.81
Mg#	-	76.2	55.4	60.1	54.7	49.4	52.0

† Hacker et al. (2015) fast Vp crustal model

‡ Hacker et al. (2015) middle crust composition = lower crust composition model

Table 5: Heat production calculation parameters

Parameter	Value
Global Surface Heat Flux	Lucazeau (2019)
Antarctica Surface Heat Flux	Shen et al. (2020)
Upper Crust Heat Production	1.65 $\mu W/m^3$ (Gaschnig et al., 2016)
Upper Crust Heat Production (cratonic)	0.8 $\mu W/m^3$ (see Discussion for source)
Average Deep Crustal Density	2900 kg/m^3 (Wipperfurth et al. (2020), this study)
Thermal Conductivity	2.65 W/(m*K) (Miao et al., 2014)

References

Artemieva, I. M. (2006). Global 1×1 thermal model TC1 for the continental lithosphere: implications for lithosphere secular evolution. *Tectonophysics*, *416*(1-4), 245–277.

Ashwal, L., Morgan, P., Kelley, S., & Percival, J. (1987). Heat production in an Archean crustal profile and implications for heat flow and mobilization of heat-producing elements. *Earth and Planetary Science Letters*, *85*(4), 439–450.

Caldwell, W. B., Klemperer, S. L., Rai, S. S., & Lawrence, J. F. (2009). Partial melt in the upper-middle crust of the northwest himalaya revealed by rayleigh wave dispersion. *Tectonophysics*, *477*(1-2), 58–65.

Cammarano, F., & Guerri, M. (2017). Global thermal models of the lithosphere. *Geophysical Journal International*, *210*(1), 56–72.

Cho, H.-M., Kim, H.-J., Jou, H.-T., Hong, J.-K., & Baag, C.-E. (2004). Transition from rifted continental to oceanic crust at the southeastern korean margin in the east sea (japan sea). *Geophysical Research Letters*, *31*(7).

Christensen, N. I., & Mooney, W. D. (1995). Seismic velocity structure and composition of the continental crust: A global view. *Journal of Geophysical Research: Solid Earth*, *100*(B6), 9761–9788.

Connolly, J. A. D. (2005). Computation of phase equilibria by linear programming: A tool for geodynamic modeling and its application to subduction zone decarbonation. *Earth and Planetary Science Letters*, *236*(1), 524-541. doi: 10.1016/j.epsl.2005.04.033

Ducea, M. N. (2011). Fingerprinting orogenic delamination. *Geology*, *39*(2), 191–192.

Fountain, D. M., Furlong, K. P., & Salisbury, M. H. (1987). A heat production model of a shield area and its implications for the heat flow-heat production relationship. *Geophysical Research Letters*, *14*(3), 283–286.

Gao, Y., Tilmann, F., van Herwaarden, D.-P., Thrastarson, S., Fichtner, A., Heit, B., ... Schurr, B. D. (2021). Full waveform inversion beneath the central andes: Insight into the dehydration of the nazca slab and delamination of the back-arc lithosphere. *Earth and Space Science Open Archive ESSOAr*.

Gaschnig, R. M., Rudnick, R. L., McDonough, W. F., Kaufman, A. J., Valley, J. W., Hu, Z., ... Beck, M. L. (2016). Compositional evolution of the upper continental crust through time, as constrained by ancient glacial diamictites. *Geochimica et Cosmochimica Acta*, *186*, 316–343.

Gohl, K. (2008). Antarctica's continent-ocean transitions: consequences for tectonic reconstructions. In *Antarctica: A keystone in a changing world: Proceedings of the 10th international symposium on antarctic earth sciences/alan k. cooper, peter barrett, howard stagg, bryan storey, edmund stump, woody wise, and the 10th isaes editorial team, polar resear* (pp. 29–38).

Gruber, B., Chacko, T., Pearson, D. G., Currie, C., & Menzies, A. (2021). Heat production and m oho temperatures in cratonic crust: evidence from lower crustal xenoliths from the slave craton. *Lithos*, *380*, 105889.

Hacker, B. R., & Abers, G. A. (2004). Subduction Factory 3: An Excel worksheet and macro for calculating the densities, seismic wave speeds, and H2O contents of minerals and rocks at pressure and temperature. *Geochemistry, Geophysics, Geosystems*, *5*(1). doi: 10.1029/2003GC000614

Hacker, B. R., Kelemen, P. B., & Behn, M. D. (2015). Continental lower crust. *Annual Review of Earth and Planetary Sciences*, *43*, 167–205.

Hartmann, J., Dürr, H. H., Moosdorf, N., Meybeck, M., & Kempe, S. (2012). The geochemical composition of the terrestrial surface (without soils) and comparison with the upper continental crust. *International Journal of Earth Sciences*, *101*(1), 365–376.

Hirata, N., Karp, B. Y., Yamaguchi, T., Kanazawa, T., Suyehiro, K., Kasahara, J., ... Kinoshita, H. (1992). Oceanic crust in the japan basin of the japan sea by the 1990 japan-ussr expedition. *Geophysical Research Letters*, *19*(20), 2027–2030.

Holland, T. J. B., & Powell, R. (2004). An internally consistent thermodynamic data set for phases of petrological interest: An Internally Consistent Thermodynamic Dataset. *Journal of Metamorphic Geology*, *16*(3), 309-343. doi: 10.1111/j.1525-1314.1998.00140.x

Huang, Y., Chubakov, V., Mantovani, F., Rudnick, R. L., & McDonough, W. F. (2013). A reference Earth model for the heat-producing elements and associated geoneutrino flux. *Geochemistry, Geophysics, Geosystems*, *14*(6), 2003-2029. doi: 10.1002/ggge.20129

Jagoutz, O., Müntener, O., Schmidt, M. W., & Burg, J.-P. (2011). The roles of flux-and decompression melting and their respective fractionation lines for continental crust formation: Evidence from the kohistan arc. *Earth and Planetary Science Letters*, *303*(1-2), 25–36.

Jagoutz, O., & Schmidt, M. W. (2012). The formation and bulk composition of modern juvenile continental crust: The kohistan arc. *Chemical Geology*, *298*, 79–96.

Jaupart, C., Mareschal, J., & Watts, A. (2007). Heat flow and thermal structure of the lithosphere. *Treatise on geophysics*, *6*, 217–252.

Jaupart, C., Mareschal, J.-C., Bouquerel, H., & Phaneuf, C. (2014). The building and stabilization of an archean craton in the superior province, canada, from a heat flow perspective. *Journal of Geophysical Research: Solid Earth*, *119*(12), 9130–9155.

Jaupart, C., Mareschal, J.-C., & Iarotsky, L. (2016). Radiogenic heat production in the continental crust. *Lithos*, *262*, 398–427.

Kay, R. W., & Kay, S. M. (1993). Delamination and delamination magmatism. *Tectonophysics*, *219*(1-3), 177–189.

Kukkonen, I., Golovanova, I., Khachay, Y. V., Druzhinin, V., Kosarev, A., & Schapov, V. (1997). Low geothermal heat flow of the urals fold belt—implication of low heat production, fluid circulation or palaeoclimate? *Tectonophysics*, *276*(1-4), 63–85.

Liu, Y.-S., Gao, S., Jin, S.-Y., Hu, S.-H., Sun, M., Zhao, Z.-B., & Feng, J.-L. (2001). Geochemistry of lower crustal xenoliths from neogene hannuoba basalt, north china craton: Implications for petrogenesis and lower crustal composition. *Geochimica et Cosmochimica Acta*, *65*(15), 2589–2604.

Lucazeau, F. (2019). Analysis and mapping of an updated terrestrial heat flow data set. *Geochemistry, Geophysics, Geosystems*, *20*(8), 4001–4024.

Mareschal, J.-C., & Jaupart, C. (2013). Radiogenic heat production, thermal regime and evolution of continental crust. *Tectonophysics*, *609*, 524–534.

McCarthy, A., Falloon, T., Sauermilch, I., Whittaker, J., Niida, K., & Green, D. (2020). Revisiting the australian-antarctic ocean-continent transition zone using petrological and geophysical characterization of exhumed subcontinental mantle. *Geochemistry, Geophysics, Geosystems*, *21*(7), e2020GC009040.

Miao, S. Q., Li, H. P., & Chen, G. (2014). Temperature dependence of thermal diffusivity, specific heat capacity, and thermal conductivity for several types of rocks. *Journal of Thermal Analysis and Calorimetry*, *115*(2), 1057–1063.

Mooney, W. D. (2015). *Crust and lithospheric structure–global crustal structure* (Vol. 1; G. Schubert, Ed.). Oxford: Elsevier.

Mooney, W. D., Laske, G., & Masters, T. G. (1998). Crust 5.1: A global crustal model at 5× 5. *Journal of Geophysical Research: Solid Earth*, *103*(B1), 727–747.

Nelson, K. D., Zhao, W., Brown, L., Kuo, J., Che, J., Liu, X., ... others (1996). Partially molten middle crust beneath southern tibet: synthesis of project indepth results. *Science*, *274*(5293), 1684–1688.

Nyblade, A. A., & Pollack, H. N. (1993). A global analysis of heat flow from precambrian terrains: implications for the thermal structure of archean and proterozoic lithosphere. *Journal of Geophysical Research: Solid Earth*, *98*(B7), 12207–12218.

Pasyanos, M. E., Masters, T. G., Laske, G., & Ma, Z. (2014). LITHO1.0: An updated crust and lithospheric model of the Earth. *Journal of Geophysical Research: Solid Earth*, *119*(3), 2153-2173. doi: 10.1002/2013JB010626

Phaneuf, C., & Mareschal, J.-C. (2014). Estimating concentrations of heat producing elements in the crust near the sudbury neutrino observatory, ontario, canada. *Tectonophysics*, *622*, 135–144.

Pinet, C., & Jaupart, C. (1987). The vertical distribution of radiogenic heat production in the precambrian crust of norway and sweden: geothermal implications. *Geophysical Research Letters*, *14*(3), 260–263.

Regis, D., Warren, C., Mottram, C. M., & Roberts, N. M. (2016). Using monazite and zircon petrochronology to constrain the P–T–t evolution of the middle crust in the bhutan himalaya. *Journal of Metamorphic Geology*, *34*(6), 617–639.

Ries, J., Bettadpur, S., Eanes, R., Kang, Z., Ko, U.-d., McCullough, C., ... others (2016). *The development and evaluation of the global gravity model ggm05* (Tech. Rep.). Center for Space Research, Report number: CSR-16-02 NASA.

Rudnick, R. L., & Gao, S. (2014). Composition of the Continental Crust. In *Treatise on Geochemistry* (p. 1-51). Elsevier. doi: 10.1016/B978-0-08-095975-7.00301-6

Rudnick, R. L., & Nyblade, A. A. (1999). The thickness and heat production of archean lithosphere: constraints from xenolith thermobarometry and surface heat flow. *Mantle petrology: field observations and high pressure experimentation: a tribute to Francis R.(Joe) Boyd*, *6*, 3–12.

Sammon, L. G., Gao, C., & McDonough, W. F. (2020). Lower crustal composition in the southwestern united states. *Journal of Geophysical Research: Solid Earth*, *125*(3), e2019JB019011.

Sammon, L. G., & McDonough, W. F. (2021). A geochemical review of amphibolite, granulite, and eclogite facies lithologies: Perspectives on the deep continental crust.

Schilling, F., & Partzsch, G. (2001). Quantifying partial melt fraction in the crust beneath the central andes and the tibetan plateau. *Physics and Chemistry of the Earth, Part A: Solid Earth and Geodesy*, *26*(4-5), 239–246.

Schmitz, M., Heinsohn, W.-D., & Schilling, F. (1997). Seismic, gravity and petrological evidence for partial melt beneath the thickened central andean crust (21–23 s). *Tectonophysics*, *270*(3-4), 313–326.

Searle, M., Cottle, J., Streule, M., & Waters, D. (2009). Crustal melt granites and migmatites along the himalaya: melt source, segregation, transport and granite emplacement mechanisms. *Earth and Environmental Science Transactions of the Royal Society of Edinburgh*, *100*(1-2), 219–233.

Semprich, J., & Simon, N. S. C. (2014). Inhibited eclogitization and consequences for geophysical rock properties and delamination models: Constraints from cratonic lower crustal xenoliths. *Gondwana Research*, *25*(2), 668-684. doi: 10.1016/j.gr.2012.08.018

Shen, W., Wiens, D. A., Lloyd, A. J., & Nyblade, A. A. (2020). A geothermal heat flux map of antarctica empirically constrained by seismic structure. *Geophysical Research Letters*, *47*(14), e2020GL086955.

Stixrude, L., & Lithgow-Bertelloni, C. (2011). Thermodynamics of mantle minerals-ii. phase equilibria. *Geophysical Journal International*, *184*(3), 1180–1213.

Szwillus, W., Afonso, J. C., Ebbing, J., & Mooney, W. D. (2019). Global crustal thickness and velocity structure from geostatistical analysis of seismic data. *Journal of*

Geophysical Research: Solid Earth, *124*(2), 1626-1652.

Wilkinson, B. H., McElroy, B. J., Kesler, S. E., Peters, S. E., & Rothman, E. D. (2009). Global geologic maps are tectonic speedometers—rates of rock cycling from area-age frequencies. *Geological Society of America Bulletin*, *121*(5-6), 760–779.

Wipperfurth, S. A., Guo, M., Šrámek, O., & McDonough, W. F. (2018). Earth's chondritic Th/U: Negligible fractionation during accretion, core formation, and crust–mantle differentiation. *Earth and Planetary Science Letters*, *498*, 196-202. doi: 10.1016/j.epsl.2018.06.029

Wipperfurth, S. A., Šrámek, O., & McDonough, W. F. (2020). Reference models for lithospheric geoneutrino signal. *Journal of Geophysical Research: Solid Earth*, *125*(2), e2019JB018433.

JOURNAL OF GEOPHYSICAL RESEARCH

Supporting Information for "The composition of the deep continental crust inferred from geochemical and geophysical data"

L. G. Sammon[1], W. F. McDonough[1,2], W. Mooney[3]

[1]Department of Geology, University of Maryland, College Park, MD 20742, USA

[2]Department of Earth Sciences and Research Center for Neutrino Science, Tohoku University, Sendai 980-8578, Japan

[3]Earthquake Science Center, United States Geological Survey, Menlo Park, CA 94025

Contents of this file

1. List of data inputs and models used to build our global deep crust model
2. Perple_X parameter settings and justification
3. Figures S1 to S18, global maps of major oxide composition at two depths

Additional Supporting Information (Files uploaded separately)

1. Collection of scripts and files for running CrustMaker
2. Global SiO_2 vs. depth model file

1. Deep Crustal Modeling

CrustMaker scripts/code - link here Geochemical Dataset - link here

USGS seismic dataset - please contact Walter Mooney at mooney@usgs.org. Global deep crust seismic data was compiled from a survey of 8000 literature based vertical seismic profiles (W. D. Mooney et al., 1998). Only profiles with both Vp and Vs were considered. The profiles were collected by various controlled and passive source methods, including refraction (reversed and unreversed), earthquake models, receiver functions, and ambient noise tomography. This data includes estimates of sediment thickness and elevation.

Global gravity anomalies from GRACE and GOCE - (Ries et al., 2016) Crustal thickness = (Pasyanos et al., 2014; Szwillus et al., 2019) Surface heat flow - (Lucazeau, 2019; Shen et al., 2020)

2. PerpleX Modeling Parameters

Parameter - *Value* - Justification

Thermodynamic data file - *Hpha02ver.dat: Holland and Powell thermodynamic database, augmented by Hacker and Abers (2004)* - Holland and Powell (2004) presents a self-consistent thermodynamic database. Hpha02ver is similar to hp02ver but is augmented by Hacker and Abers (2004) to be consistent with the α - β quartz transition. Another option, Hp11ver.dat, does not include shear moduli and thus cannot be used to calculate Vs. The Stx11ver.dat database uses the Stixrude and Lithgow-Bertelloni (2011) method for calculating elastic moduli, but only considers major mantle phases.

Solution models - *N/A* - No solution models were included. Including solution models increases the calculation time 13-fold. The difference between results when not including solution models vs. including Holland & Powell (HP) solution models averages to 0.1 km/s in Vp, <0.1 km/s in Vs, and <0.01 in Vp/Vs. Future tests including solution models can report on the accuracy of mineral endmember solutions, but this does not measurably change bulk rock and bulk crustal properties.

Amphibolite Volatiles - *1 wt.%* - The median amount of H_2O in amphibolite samples (N = 285) was found to be 1.2 $\pm$ 0.6 wt.%. 1 wt.% was chosen as a starting point calculation. Further calculations can be done with 0.5 wt.% and 1.5 wt.% water.

Pressure Range - *1,500 - 30,000 bars (0.15 - 3.0 GPa)* - This range translates to depths from about 5km to 100km, which encompasses the amphibolite and granulite stability fields and expected deep crustal depths up to Himalayan thickness.

Temperature Range - *300 - 1800 K (27 - 1,027°C)* - Temperatures below 770 K covers near-surface temperatures to the amphibolite stability field, in case amphibolites exist in the middle crust in disequilibrium. 800 - 1300 K encompasses the stability field for granulite. 300 - 800 covers all possibilities from near-surface temperatures to the granulite wet solidus. Granulites existing in this range would be at thermodynamic disequilibrium, but retrograde metamorphosis is unlikely. Granulite facies metamorphosis is marked by the dehydration of hydrous minerals. Rehydration is difficult, making rehydration unlikely to occur (Semprich & Simon, 2014). 1800 K sets the (very hot) maximum temperature cap to again account for possible temperatures in Himalayan crust and also to allow room for experimentation with temperature.

Granulite Volatiles - *0 wt.%* - Granulite is characterized by the dehydration of hydrous minerals.

3. Major Oxide Maps

References

Artemieva, I. M. (2006). Global 1×1 thermal model TC1 for the continental lithosphere: implications for lithosphere secular evolution. *Tectonophysics*, *416*(1-4), 245–277.

Ashwal, L., Morgan, P., Kelley, S., & Percival, J. (1987). Heat production in an Archean crustal profile and implications for heat flow and mobilization of heat-producing elements. *Earth and Planetary Science Letters*, *85*(4), 439–450.

Caldwell, W. B., Klemperer, S. L., Rai, S. S., & Lawrence, J. F. (2009). Partial melt in the upper-middle crust of the northwest himalaya revealed by rayleigh wave dispersion. *Tectonophysics*, *477*(1-2), 58–65.

Cammarano, F., & Guerri, M. (2017). Global thermal models of the lithosphere. *Geophysical Journal International*, *210*(1), 56–72.

Cho, H.-M., Kim, H.-J., Jou, H.-T., Hong, J.-K., & Baag, C.-E. (2004). Transition from rifted continental to oceanic crust at the southeastern korean margin in the east sea (japan sea). *Geophysical Research Letters*, *31*(7).

Christensen, N. I., & Mooney, W. D. (1995). Seismic velocity structure and composition of the continental crust: A global view. *Journal of Geophysical Research: Solid Earth*, *100*(B6), 9761–9788.

Connolly, J. A. D. (2005). Computation of phase equilibria by linear programming: A tool for geodynamic modeling and its application to subduction zone decarbonation. *Earth and Planetary Science Letters*, *236*(1), 524-541. doi: 10.1016/j.epsl.2005.04.033

Ducea, M. N. (2011). Fingerprinting orogenic delamination. *Geology*, *39*(2), 191–192.

Fountain, D. M., Furlong, K. P., & Salisbury, M. H. (1987). A heat production model of a shield area and its implications for the heat flow-heat production relationship. *Geophysical Research Letters*, *14*(3), 283–286.

Gao, Y., Tilmann, F., van Herwaarden, D.-P., Thrastarson, S., Fichtner, A., Heit, B., ... Schurr, B. D. (2021). Full waveform inversion beneath the central andes: Insight into the dehydration of the nazca slab and delamination of the back-arc lithosphere. *Earth and Space Science Open Archive ESSOAr*.

Gaschnig, R. M., Rudnick, R. L., McDonough, W. F., Kaufman, A. J., Valley, J. W., Hu, Z., ... Beck, M. L. (2016). Compositional evolution of the upper continental crust through time, as constrained by ancient glacial diamictites. *Geochimica et Cosmochimica Acta*, *186*, 316–343.

Gohl, K. (2008). Antarctica's continent-ocean transitions: consequences for tectonic reconstructions. In *Antarctica: A keystone in a changing world: Proceedings of the 10th international symposium on antarctic earth sciences/alan k. cooper, peter barrett, howard stagg, bryan storey, edmund stump, woody wise, and the 10th isaes editorial team, polar resear* (pp. 29–38).

Gruber, B., Chacko, T., Pearson, D. G., Currie, C., & Menzies, A. (2021). Heat production and m oho temperatures in cratonic crust: evidence from lower crustal xenoliths from the slave craton. *Lithos*, *380*, 105889.

Hacker, B. R., & Abers, G. A. (2004). Subduction Factory 3: An Excel worksheet and macro for calculating the densities, seismic wave speeds, and H2O contents of minerals and rocks at pressure and temperature. *Geochemistry, Geophysics, Geosystems*, *5*(1). doi: 10.1029/2003GC000614

Hacker, B. R., Kelemen, P. B., & Behn, M. D. (2015). Continental lower crust. *Annual*

Review of Earth and Planetary Sciences, *43*, 167–205.

Hartmann, J., Dürr, H. H., Moosdorf, N., Meybeck, M., & Kempe, S. (2012). The geochemical composition of the terrestrial surface (without soils) and comparison with the upper continental crust. *International Journal of Earth Sciences*, *101*(1), 365–376.

Hirata, N., Karp, B. Y., Yamaguchi, T., Kanazawa, T., Suyehiro, K., Kasahara, J., ... Kinoshita, H. (1992). Oceanic crust in the japan basin of the japan sea by the 1990 japan-ussr expedition. *Geophysical Research Letters*, *19*(20), 2027–2030.

Holland, T. J. B., & Powell, R. (2004). An internally consistent thermodynamic data set for phases of petrological interest: An Internally Consistent Thermodynamic Dataset. *Journal of Metamorphic Geology*, *16*(3), 309-343. doi: 10.1111/j.1525-1314.1998.00140.x

Huang, Y., Chubakov, V., Mantovani, F., Rudnick, R. L., & McDonough, W. F. (2013). A reference Earth model for the heat-producing elements and associated geoneutrino flux. *Geochemistry, Geophysics, Geosystems*, *14*(6), 2003-2029. doi: 10.1002/ggge.20129

Jagoutz, O., Müntener, O., Schmidt, M. W., & Burg, J.-P. (2011). The roles of flux-and decompression melting and their respective fractionation lines for continental crust formation: Evidence from the kohistan arc. *Earth and Planetary Science Letters*, *303*(1-2), 25–36.

Jagoutz, O., & Schmidt, M. W. (2012). The formation and bulk composition of modern juvenile continental crust: The kohistan arc. *Chemical Geology*, *298*, 79–96.

Jaupart, C., Mareschal, J., & Watts, A. (2007). Heat flow and thermal structure of the lithosphere. *Treatise on geophysics*, *6*, 217–252.

Jaupart, C., Mareschal, J.-C., Bouquerel, H., & Phaneuf, C. (2014). The building and stabilization of an archean craton in the superior province, canada, from a heat flow perspective. *Journal of Geophysical Research: Solid Earth*, *119*(12), 9130–9155.

Jaupart, C., Mareschal, J.-C., & Iarotsky, L. (2016). Radiogenic heat production in the continental crust. *Lithos*, *262*, 398–427.

Kay, R. W., & Kay, S. M. (1993). Delamination and delamination magmatism. *Tectonophysics*, *219*(1-3), 177–189.

Kukkonen, I., Golovanova, I., Khachay, Y. V., Druzhinin, V., Kosarev, A., & Schapov, V. (1997). Low geothermal heat flow of the urals fold belt—implication of low heat production, fluid circulation or palaeoclimate? *Tectonophysics*, *276*(1-4), 63–85.

Liu, Y.-S., Gao, S., Jin, S.-Y., Hu, S.-H., Sun, M., Zhao, Z.-B., & Feng, J.-L. (2001). Geochemistry of lower crustal xenoliths from neogene hannuoba basalt, north china craton: Implications for petrogenesis and lower crustal composition. *Geochimica et Cosmochimica Acta*, *65*(15), 2589–2604.

Lucazeau, F. (2019). Analysis and mapping of an updated terrestrial heat flow data set. *Geochemistry, Geophysics, Geosystems*, *20*(8), 4001–4024.

Mareschal, J.-C., & Jaupart, C. (2013). Radiogenic heat production, thermal regime and evolution of continental crust. *Tectonophysics*, *609*, 524–534.

McCarthy, A., Falloon, T., Sauermilch, I., Whittaker, J., Niida, K., & Green, D. (2020). Revisiting the australian-antarctic ocean-continent transition zone using petrological and geophysical characterization of exhumed subcontinental mantle. *Geochemistry, Geophysics, Geosystems*, *21*(7), e2020GC009040.

Miao, S. Q., Li, H. P., & Chen, G. (2014). Temperature dependence of thermal diffusivity, specific heat capacity, and thermal conductivity for several types of rocks. *Journal of Thermal Analysis and Calorimetry*, *115*(2), 1057–1063.

Mooney, W. (2015). *Global crustal structure* (G. Schubert, Ed.). Elsevier.

Mooney, W. D., Laske, G., & Masters, T. G. (1998). Crust 5.1: A global crustal model at 5× 5. *Journal of Geophysical Research: Solid Earth*, *103*(B1), 727–747.

Nelson, K. D., Zhao, W., Brown, L., Kuo, J., Che, J., Liu, X., … others (1996). Partially molten middle crust beneath southern tibet: synthesis of project indepth results. *Science*, *274*(5293), 1684–1688.

Nyblade, A. A., & Pollack, H. N. (1993). A global analysis of heat flow from precambrian terrains: implications for the thermal structure of archean and proterozoic lithosphere. *Journal of Geophysical Research: Solid Earth*, *98*(B7), 12207–12218.

Pasyanos, M. E., Masters, T. G., Laske, G., & Ma, Z. (2014). LITHO1.0: An updated crust and lithospheric model of the Earth. *Journal of Geophysical Research: Solid Earth*, *119*(3), 2153-2173. doi: 10.1002/2013JB010626

Phaneuf, C., & Mareschal, J.-C. (2014). Estimating concentrations of heat producing elements in the crust near the sudbury neutrino observatory, ontario, canada. *Tectonophysics*, *622*, 135–144.

Pinet, C., & Jaupart, C. (1987). The vertical distribution of radiogenic heat production in the precambrian crust of norway and sweden: geothermal implications. *Geophysical Research Letters*, *14*(3), 260–263.

Regis, D., Warren, C., Mottram, C. M., & Roberts, N. M. (2016). Using monazite and zircon petrochronology to constrain the P–T–t evolution of the middle crust in the bhutan himalaya. *Journal of Metamorphic Geology*, *34*(6), 617–639.

Ries, J., Bettadpur, S., Eanes, R., Kang, Z., Ko, U.-d., McCullough, C., ... others (2016). *The development and evaluation of the global gravity model ggm05* (Tech. Rep.). Center for Space Research, Report number: CSR-16-02 NASA.

Rudnick, R. L., & Gao, S. (2014). Composition of the Continental Crust. In *Treatise on Geochemistry* (p. 1-51). Elsevier. doi: 10.1016/B978-0-08-095975-7.00301-6

Rudnick, R. L., & Nyblade, A. A. (1999). The thickness and heat production of archean lithosphere: constraints from xenolith thermobarometry and surface heat flow. *Mantle petrology: field observations and high pressure experimentation: a tribute to Francis R.(Joe) Boyd*, *6*, 3–12.

Sammon, L. G., Gao, C., & McDonough, W. F. (2020). Lower crustal composition in the southwestern united states. *Journal of Geophysical Research: Solid Earth*, *125*(3), e2019JB019011.

Sammon, L. G., & McDonough, W. F. (2021). A geochemical review of amphibolite, granulite, and eclogite facies lithologies: Perspectives on the deep continental crust.

Schilling, F., & Partzsch, G. (2001). Quantifying partial melt fraction in the crust beneath the central andes and the tibetan plateau. *Physics and Chemistry of the Earth, Part A: Solid Earth and Geodesy*, *26*(4-5), 239–246.

Schmitz, M., Heinsohn, W.-D., & Schilling, F. (1997). Seismic, gravity and petrological evidence for partial melt beneath the thickened central andean crust (21–23 s). *Tectonophysics*, *270*(3-4), 313–326.

Searle, M., Cottle, J., Streule, M., & Waters, D. (2009). Crustal melt granites and migmatites along the himalaya: melt source, segregation, transport and granite emplacement mechanisms. *Earth and Environmental Science Transactions of the Royal Society of Edinburgh*, *100*(1-2), 219–233.

Semprich, J., & Simon, N. S. C. (2014). Inhibited eclogitization and consequences for geophysical rock properties and delamination models: Constraints from cratonic lower crustal xenoliths. *Gondwana Research*, *25*(2), 668-684. doi: 10.1016/j.gr.2012.08.018

Shen, W., Wiens, D. A., Lloyd, A. J., & Nyblade, A. A. (2020). A geothermal heat flux map of antarctica empirically constrained by seismic structure. *Geophysical Research Letters*, *47*(14), e2020GL086955.

Stixrude, L., & Lithgow-Bertelloni, C. (2011). Thermodynamics of mantle minerals-ii. phase equilibria. *Geophysical Journal International*, *184*(3), 1180–1213.

Szwillus, W., Afonso, J. C., Ebbing, J., & Mooney, W. D. (2019). Global crustal thickness and velocity structure from geostatistical analysis of seismic data. *Journal of Geophysical Research: Solid Earth*, *124*(2), 1626-1652.

Wilkinson, B. H., McElroy, B. J., Kesler, S. E., Peters, S. E., & Rothman, E. D. (2009). Global geologic maps are tectonic speedometers—rates of rock cycling from area-age frequencies. *Geological Society of America Bulletin*, *121*(5-6), 760–779.

Wipperfurth, S. A., Guo, M., Šrámek, O., & McDonough, W. F. (2018). Earth's chondritic Th/U: Negligible fractionation during accretion, core formation, and crust–mantle differentiation. *Earth and Planetary Science Letters*, *498*, 196-202. doi: 10.1016/j.epsl.2018.06.029

Wipperfurth, S. A., Šrámek, O., & McDonough, W. F. (2020). Reference models for lithospheric geoneutrino signal. *Journal of Geophysical Research: Solid Earth*, *125*(2), e2019JB018433.

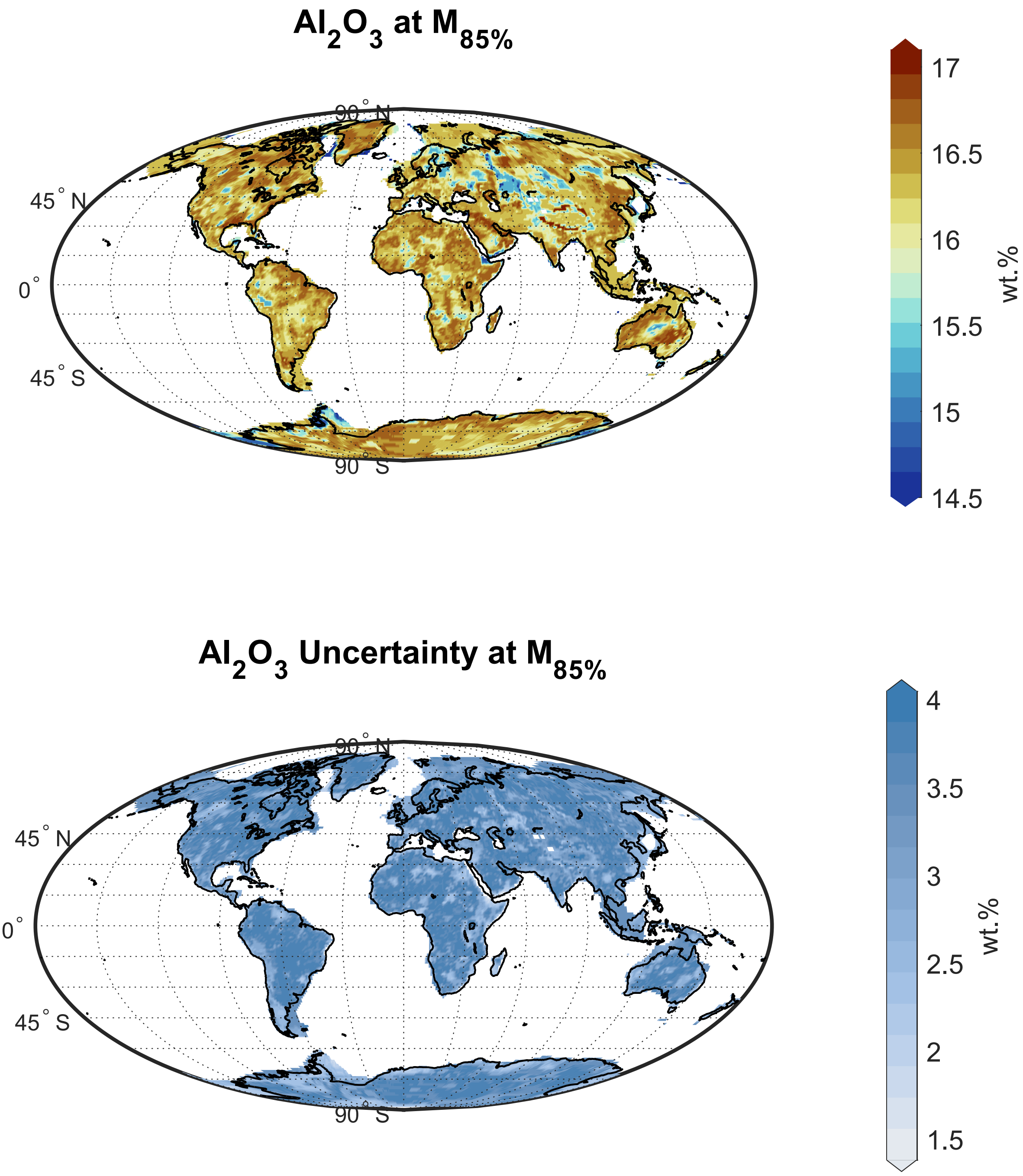
Al_2O_3 at $M_{85\%}$
90° N
45° N
0°
45° S
90° S
17
16.5
16
15.5
15
14.5
wt.%
Al_2O_3 Uncertainty at $M_{85\%}$
90° N
45° N
0°
45° S
90° S
4
3.5
3
2.5
2
1.5
wt.%

Figure S1.

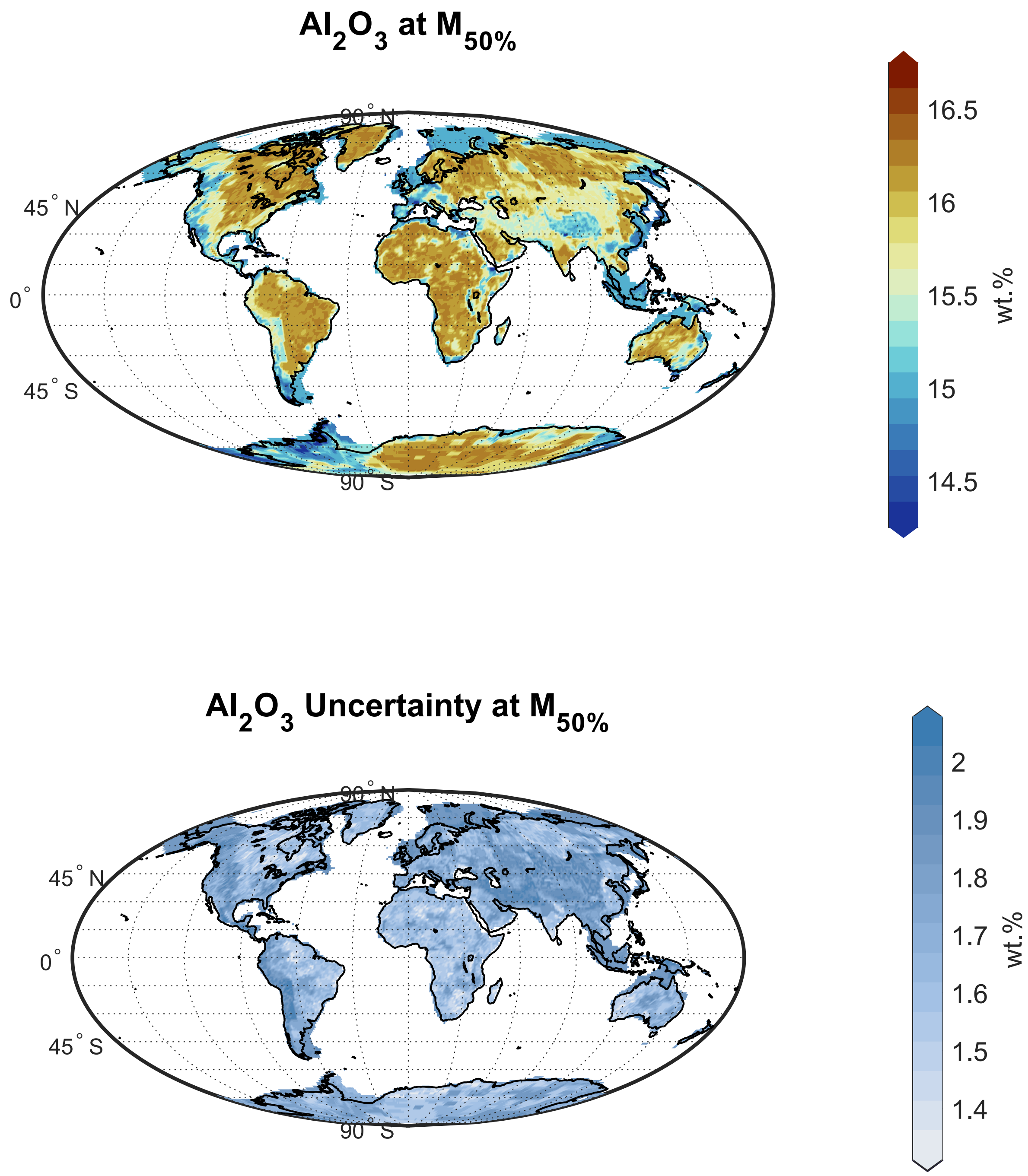
Al_2O_3 at $M_{50\%}$
90° N
45° N
0°
45° S
90° S
16.5
16
15.5
15
14.5
wt.%
Al_2O_3 Uncertainty at $M_{50\%}$
90° N
45° N
0°
45° S
90° S
2
1.9
1.8
1.7
1.6
1.5
1.4
wt.%

Figure S2.

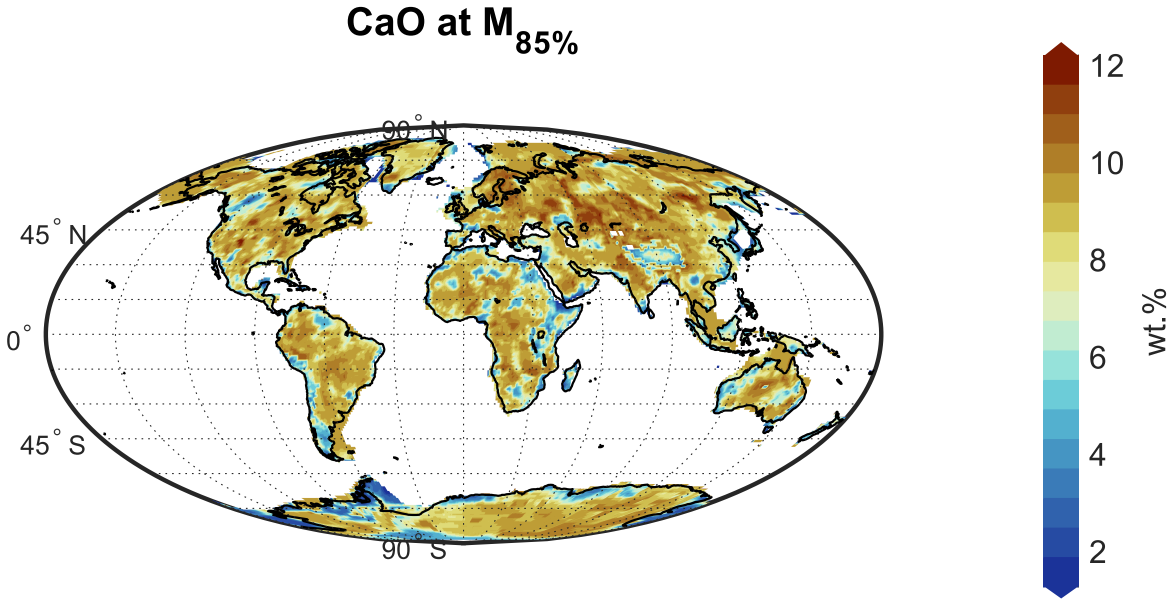
CaO at M85%
90° N
45° N
0°
45° S
90° S
12
10
8
6
4
2
wt.%

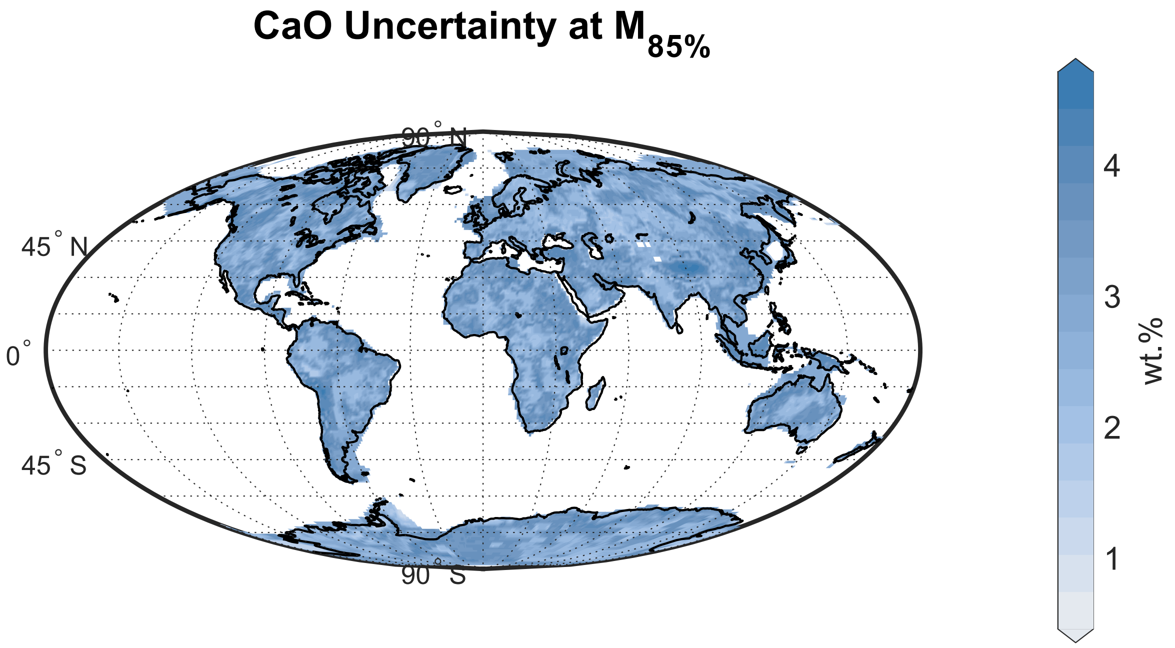
CaO Uncertainty at M85%
90° N
45° N
0°
45° S
90° S
4
3
2
1
wt.%

Figure S3.

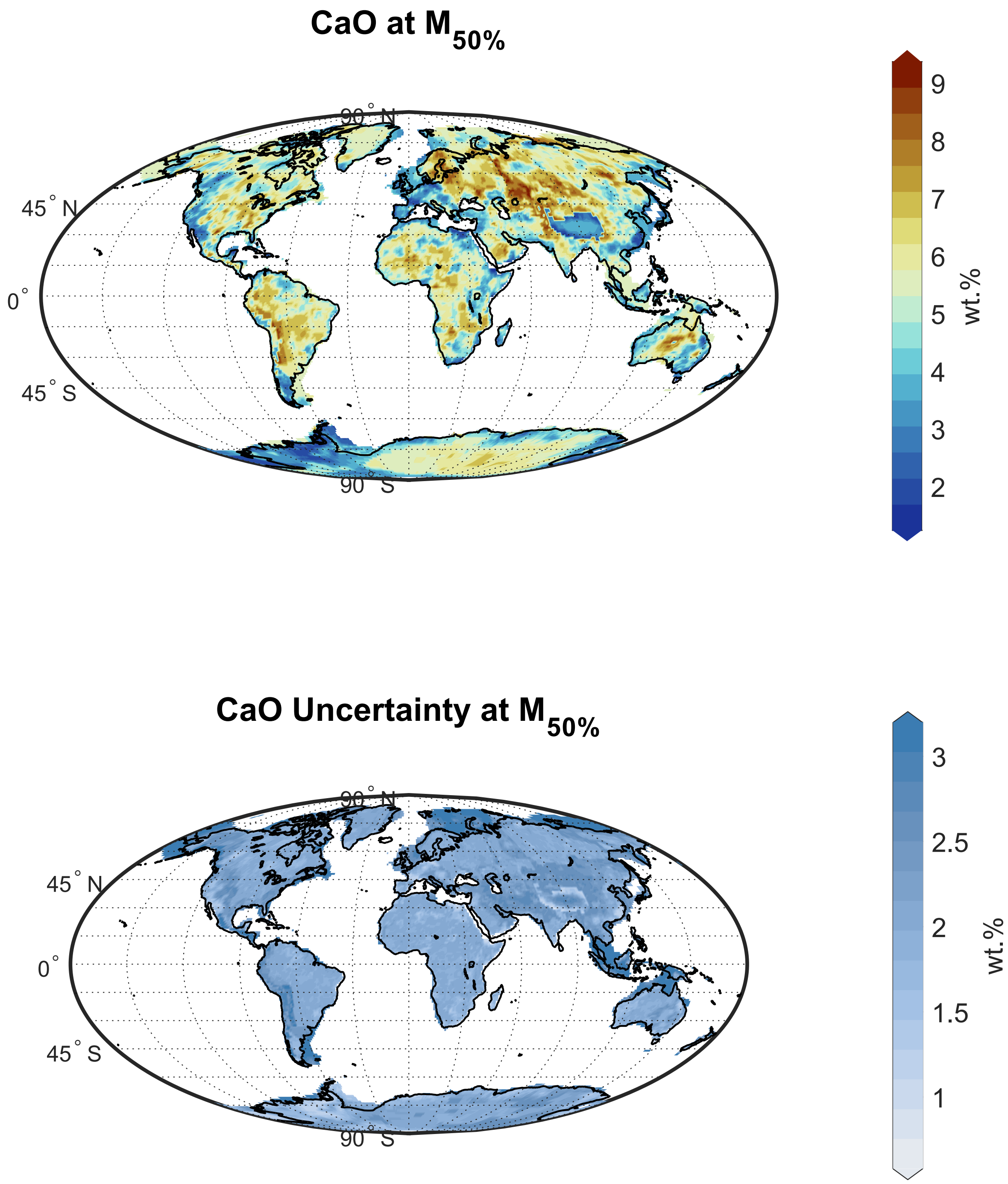
CaO at $M_{50\%}$
90° N
45° N
0°
45° S
90° S
9
8
7
6
5
4
3
2
wt.%
CaO Uncertainty at $M_{50\%}$
90° N
45° N
0°
45° S
90° S
3
2.5
2
1.5
1
wt.%

Figure S4.

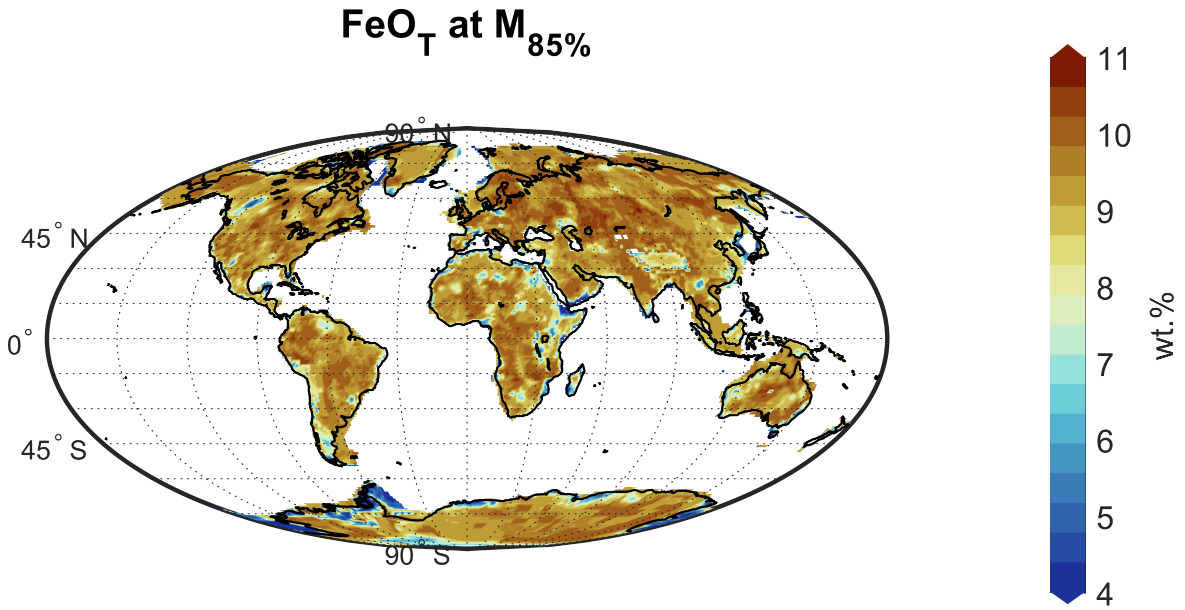
FeO$_T$ at M$_{85\%}$
90° N
45° N
0°
45° S
90° S
11
10
9
8
7
6
5
4
wt.%

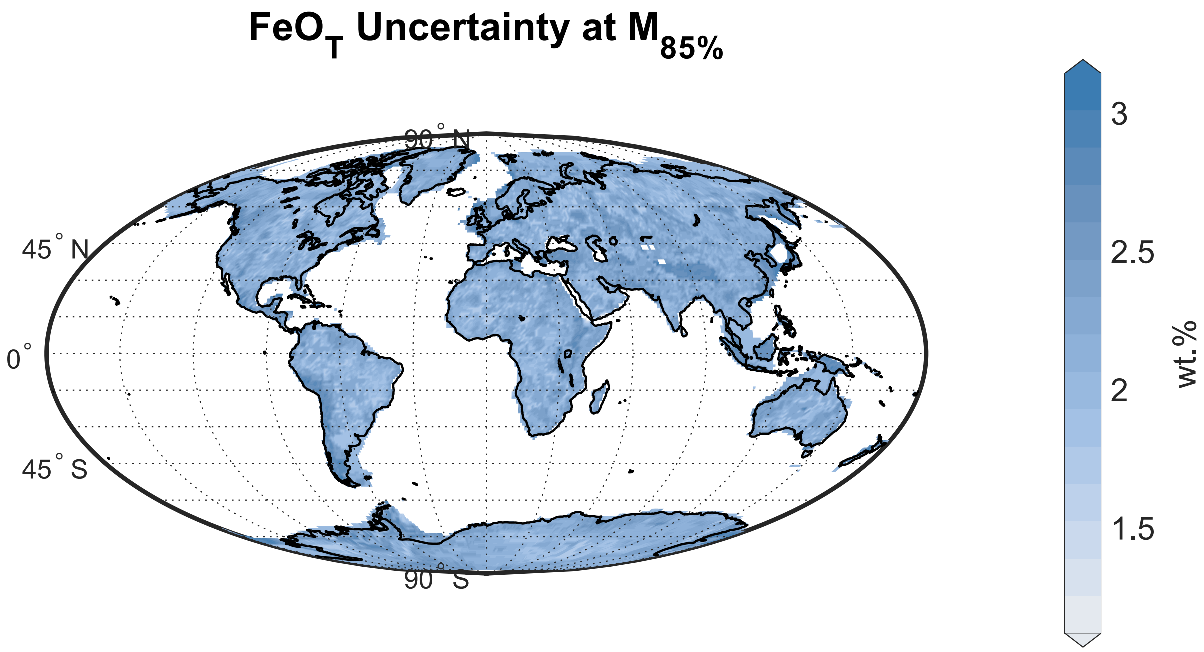
FeO$_T$ Uncertainty at M$_{85\%}$
90° N
45° N
0°
45° S
90° S
3
2.5
2
1.5
wt.%

Figure S5.

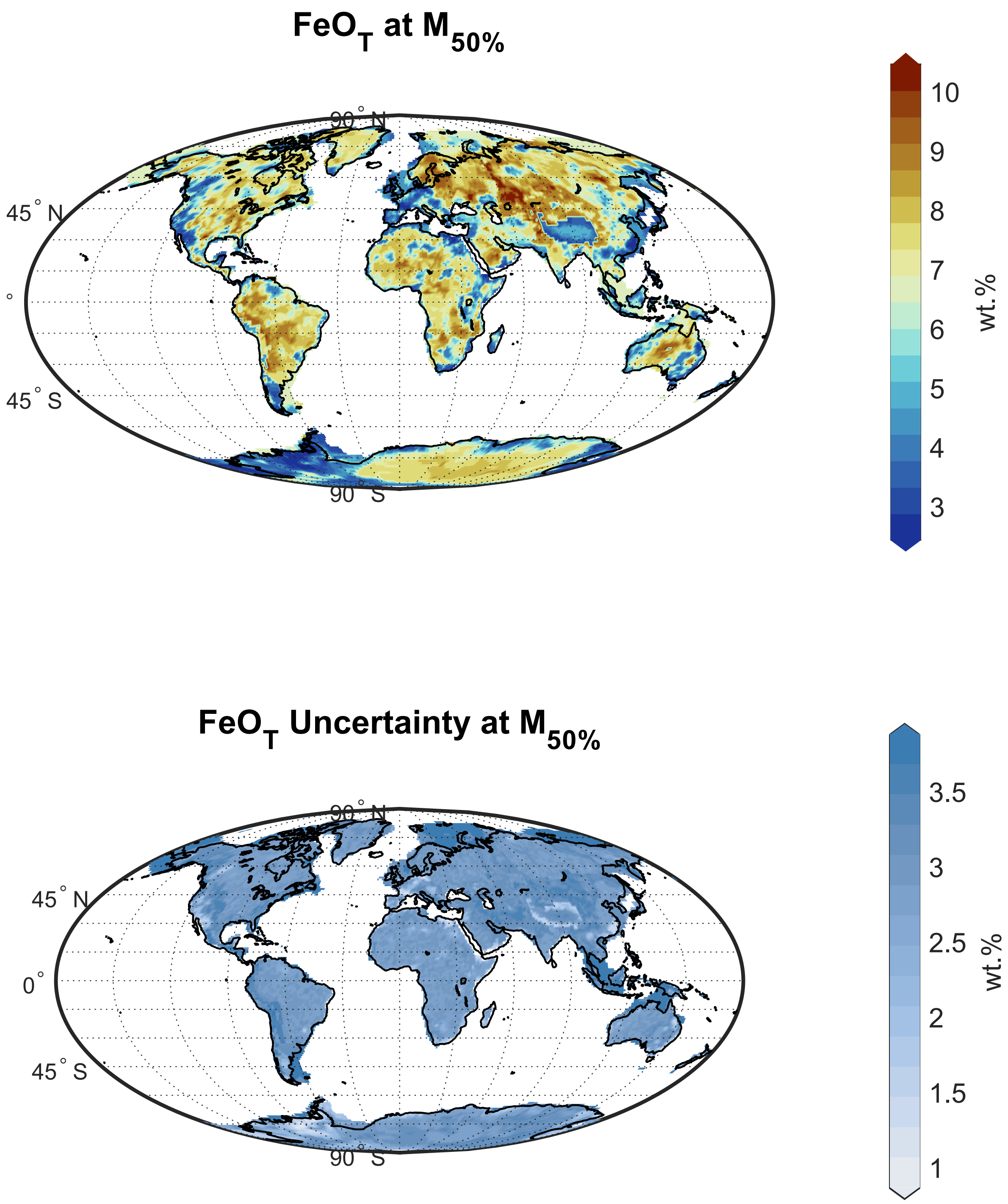
FeO_T at M_50%
90° N
45° N
°
45° S
90° S
10
9
8
7
6
5
4
3
wt.%
FeO_T Uncertainty at M_50%
90° N
45° N
0°
45° S
90° S
3.5
3
2.5
2
1.5
1
wt.%

Figure S6.

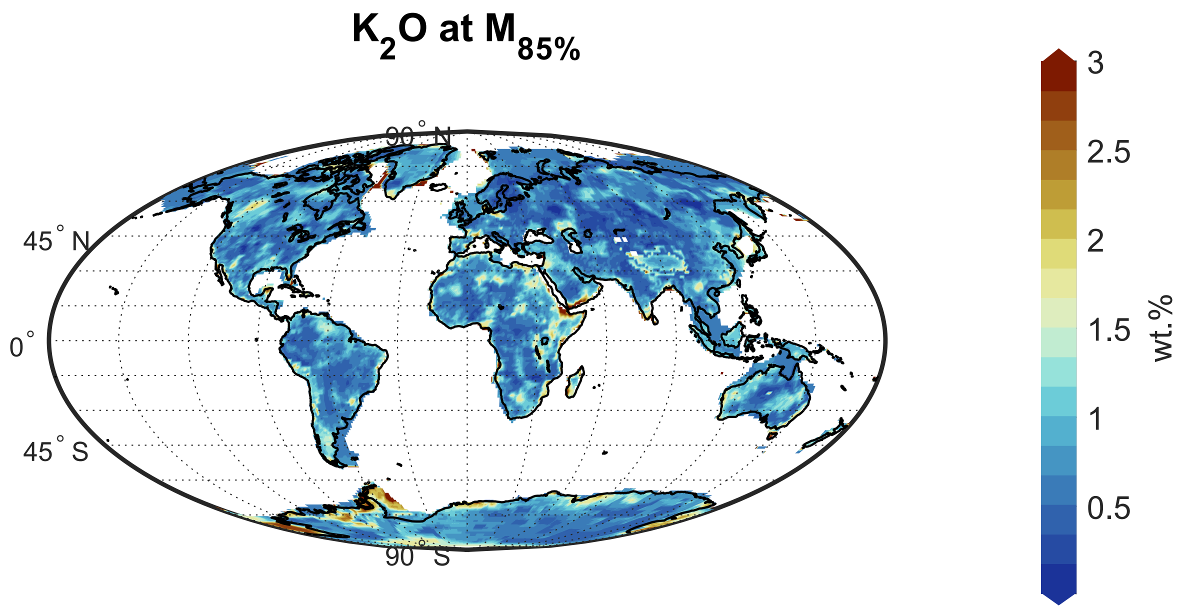
K_2O at $M_{85\%}$
90° N
45° N
0°
45° S
90° S
3
2.5
2
1.5
1
0.5
wt.%

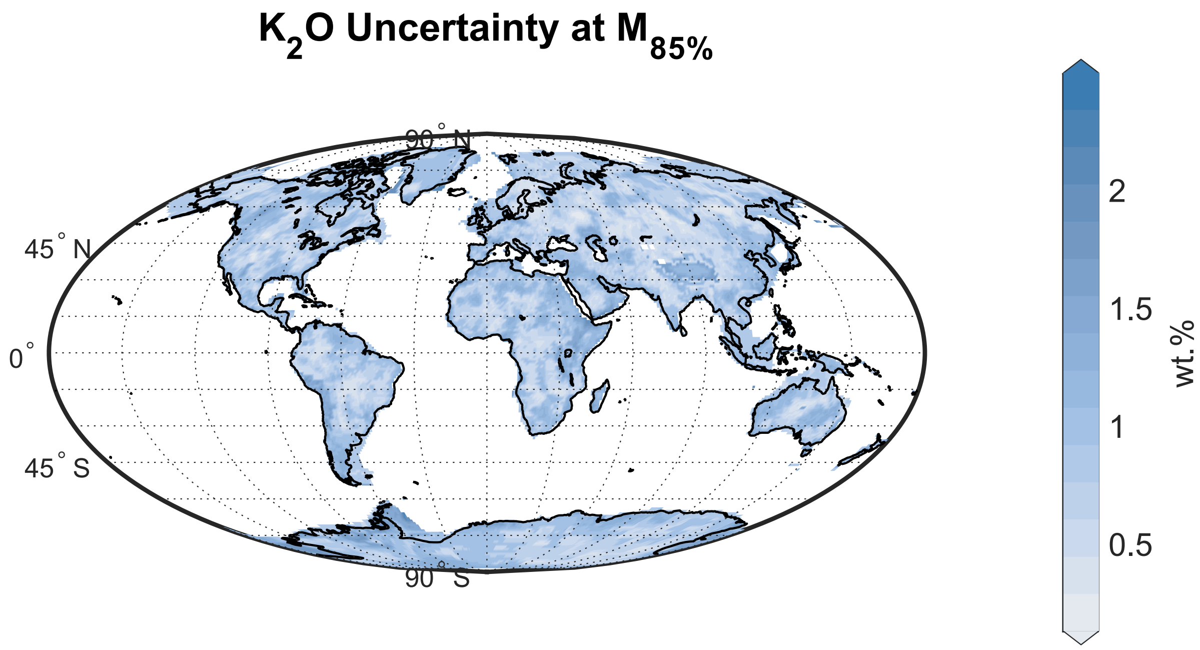
K_2O Uncertainty at $M_{85\%}$
90° N
45° N
0°
45° S
90° S
2
1.5
1
0.5
wt.%

Figure S7.

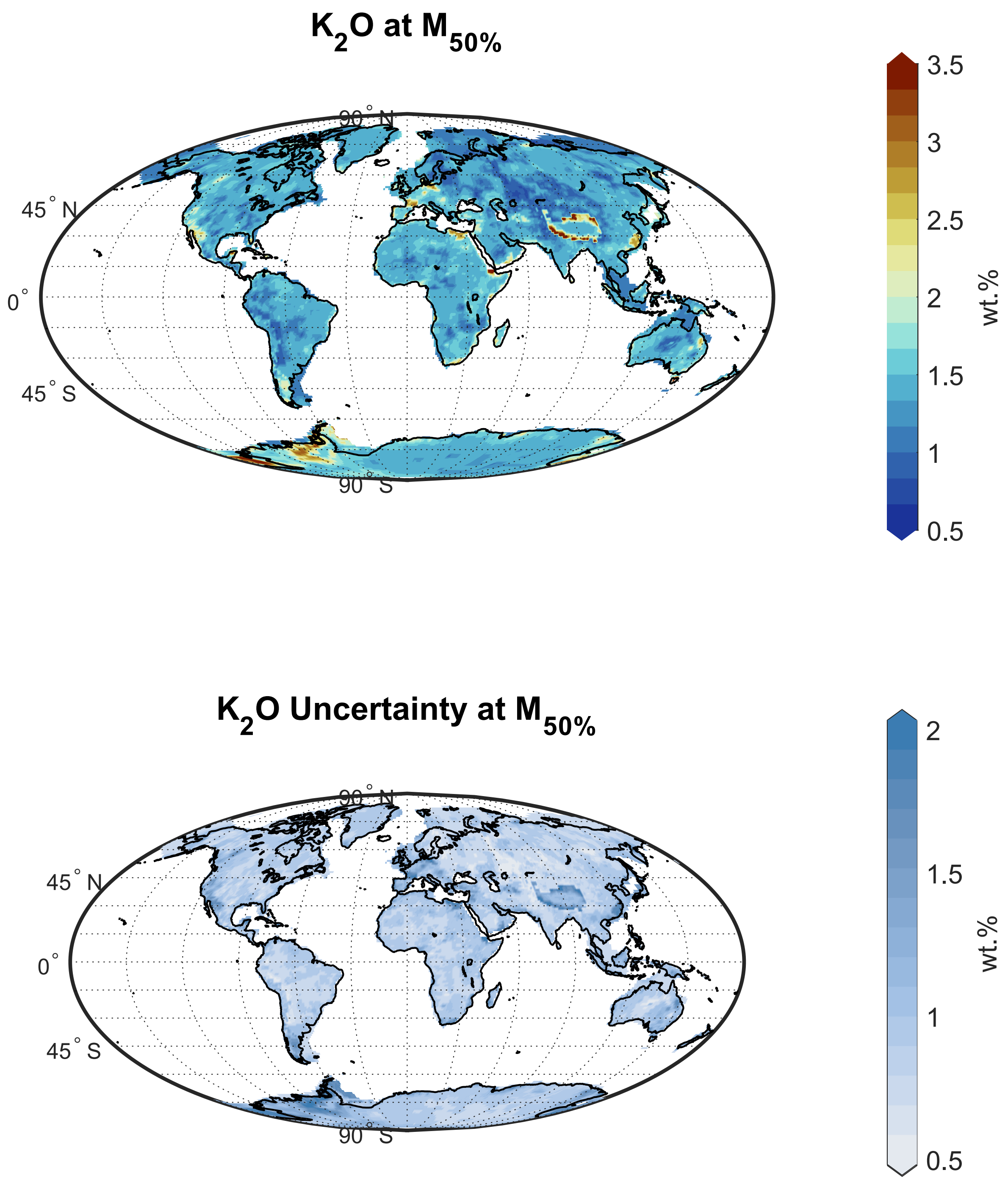
K2O at M50%
90° N
45° N
0°
45° S
90° S
3.5
3
2.5
2
1.5
1
0.5
wt.%
K2O Uncertainty at M50%
90° N
45° N
0°
45° S
90° S
2
1.5
1
0.5
wt.%

Figure S8.

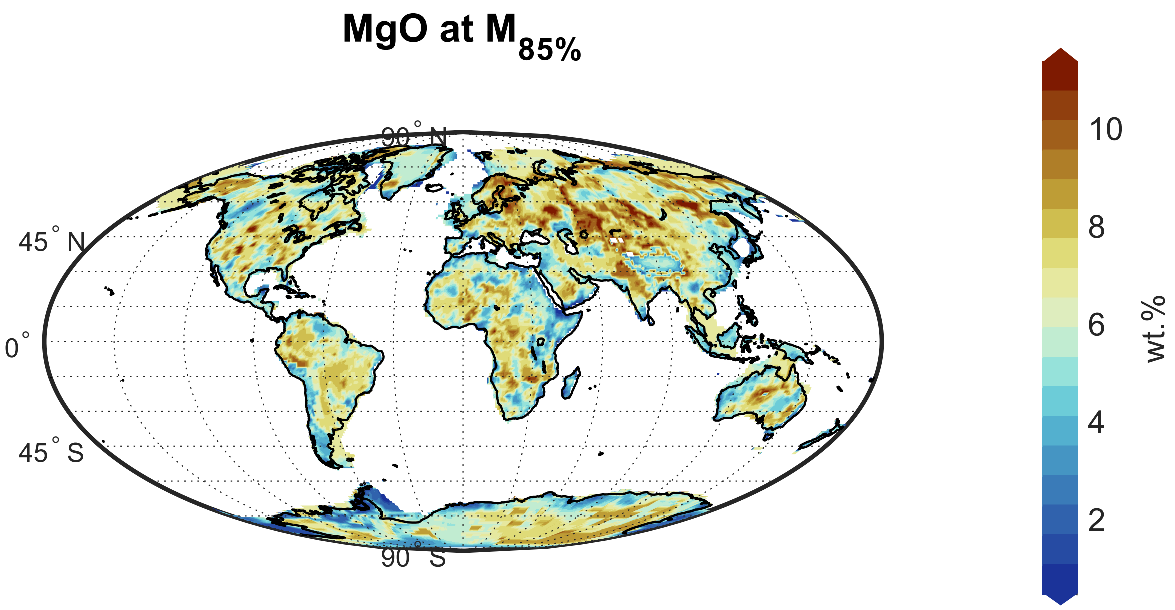
MgO at $M_{85\%}$
90° N
45° N
0°
45° S
90° S
10
8
6
4
2
wt.%

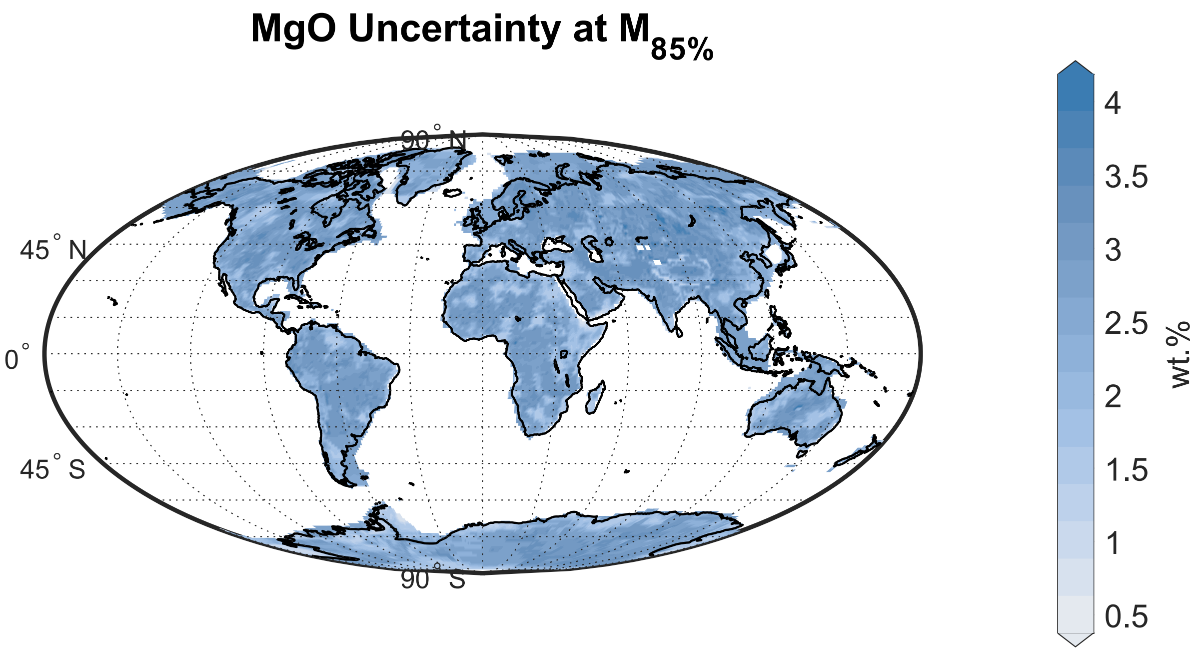
MgO Uncertainty at $M_{85\%}$
90° N
45° N
0°
45° S
90° S
4
3.5
3
2.5
2
1.5
1
0.5
wt.%

Figure S9.

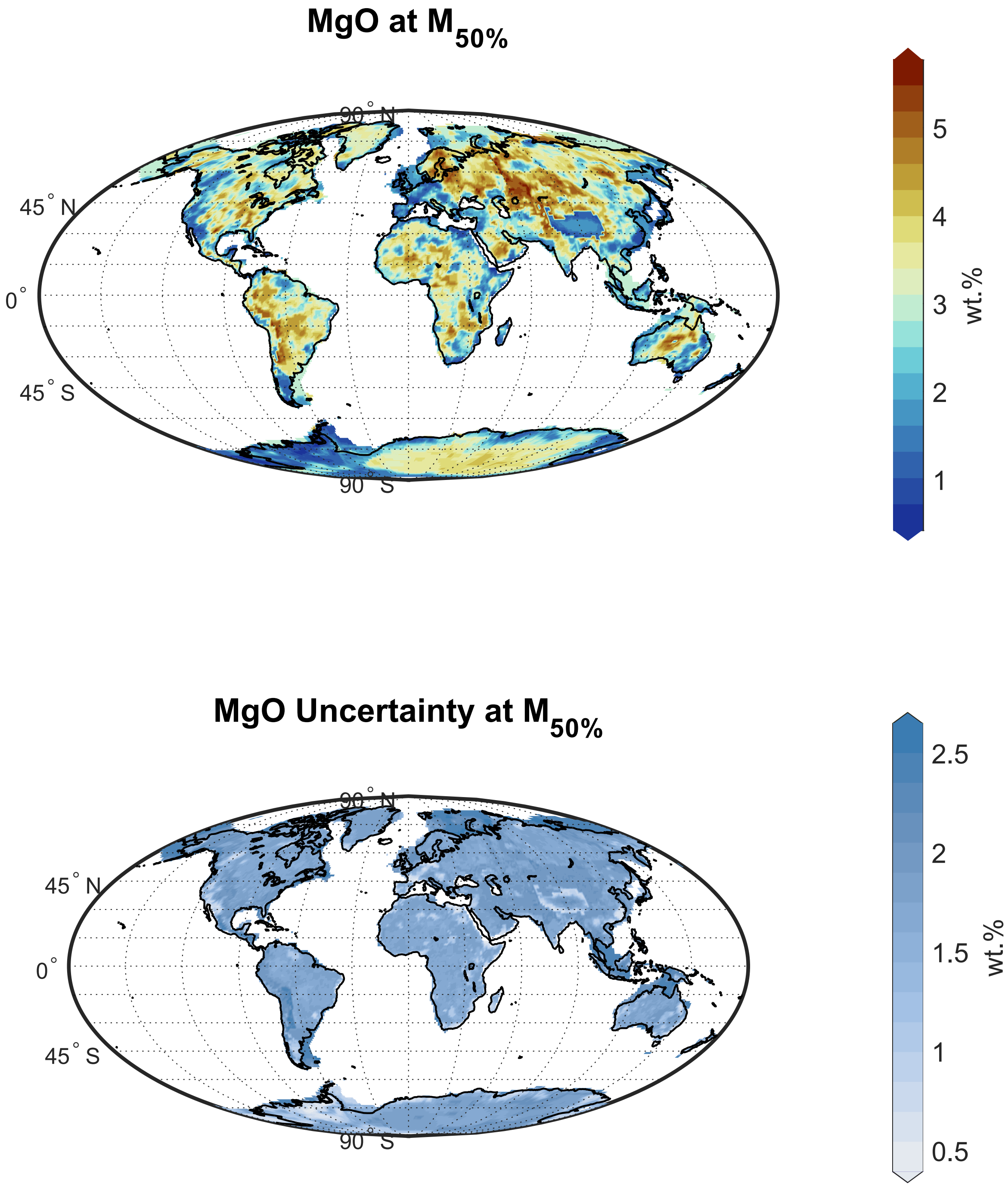
MgO at $M_{50\%}$
90° N
45° N
0°
45° S
90° S
5
4
3
2
1
wt.%
MgO Uncertainty at $M_{50\%}$
90° N
45° N
0°
45° S
90° S
2.5
2
1.5
1
0.5
wt.%

Figure S10.

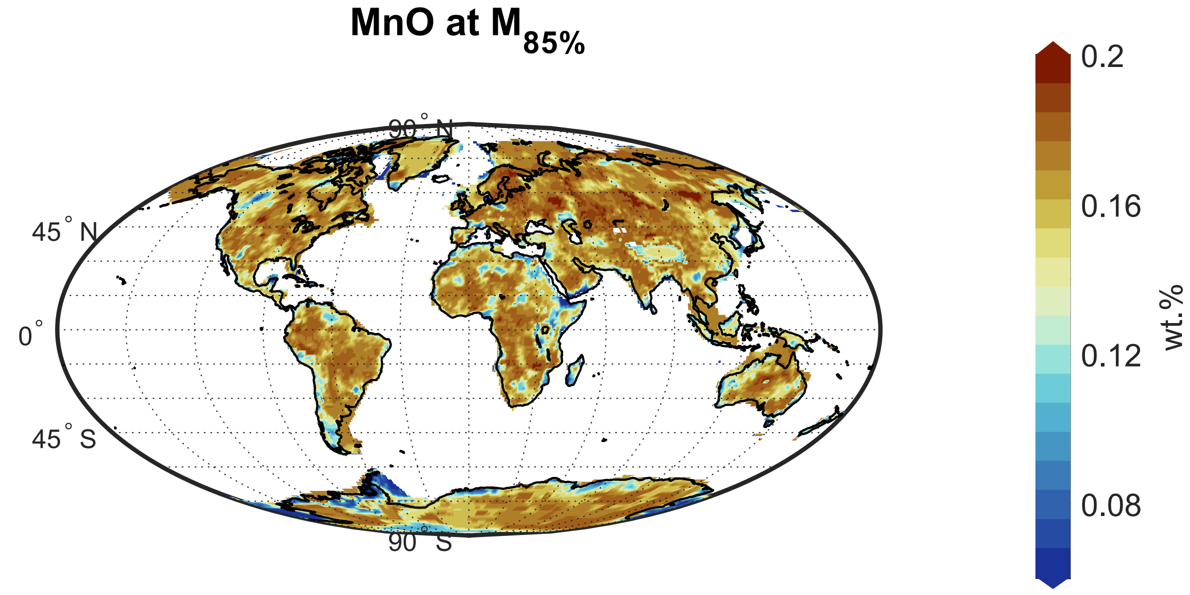
MnO at M85%
90° N
45° N
0°
45° S
90° S
0.2
0.16
0.12
0.08
wt.%

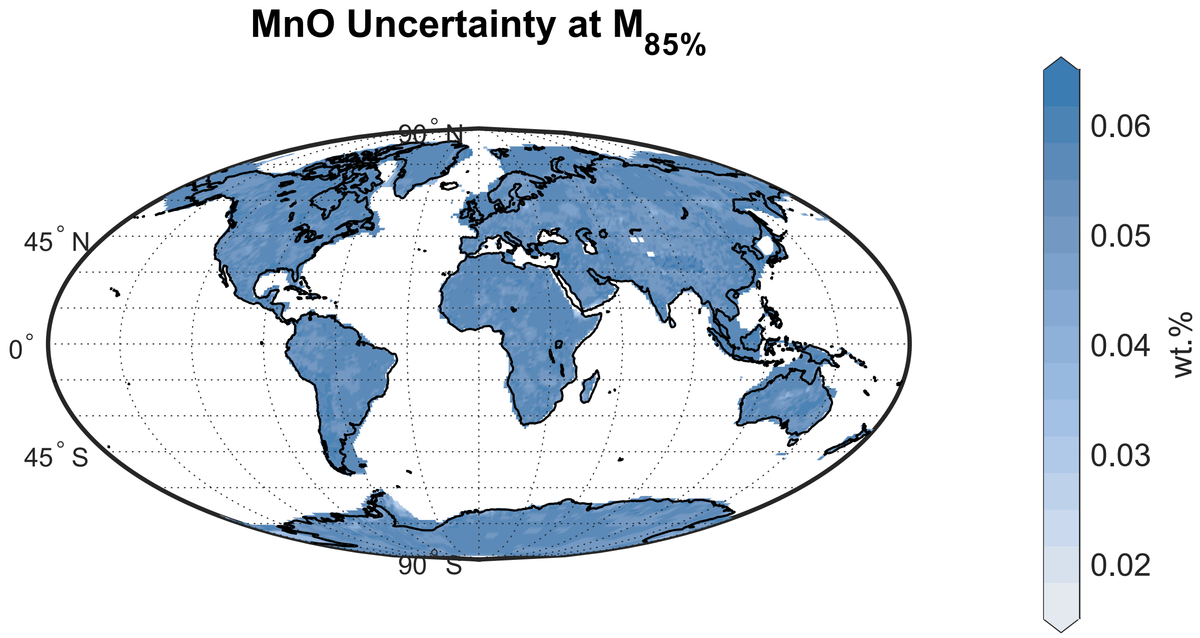
MnO Uncertainty at M85%
90° N
45° N
0°
45° S
90° S
0.06
0.05
0.04
0.03
0.02
wt.%

Figure S11.

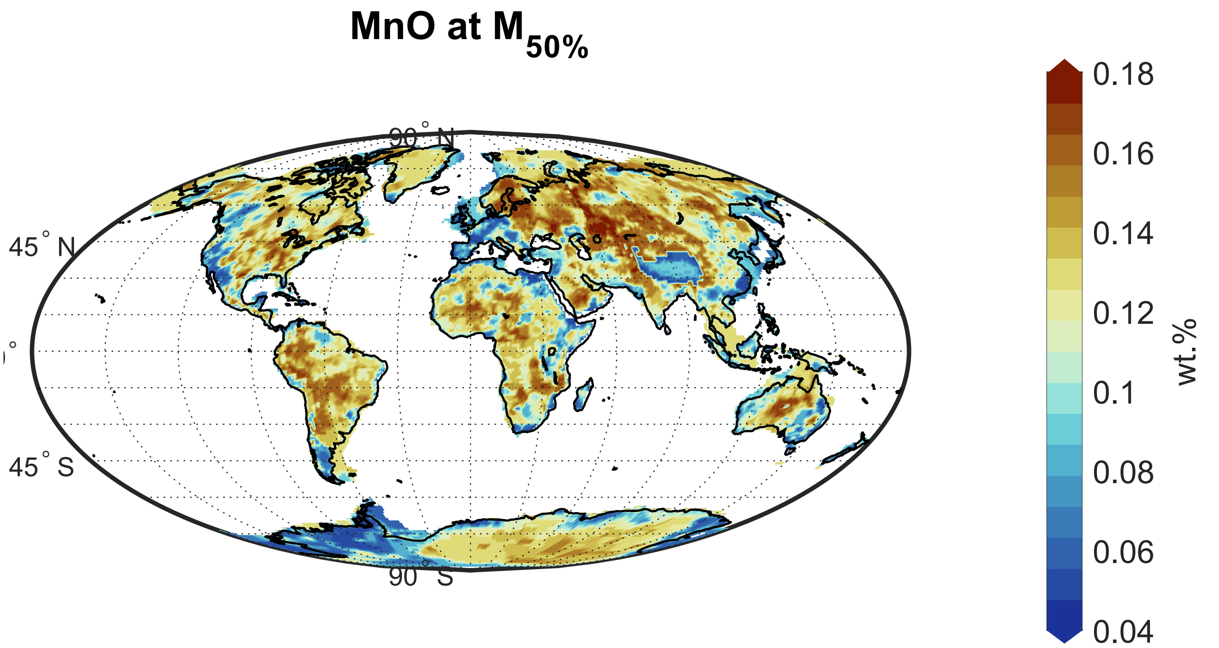
MnO at $M_{50\%}$
90° N
45° N
0°
45° S
90° S
0.18
0.16
0.14
0.12
0.1
0.08
0.06
0.04
wt.%

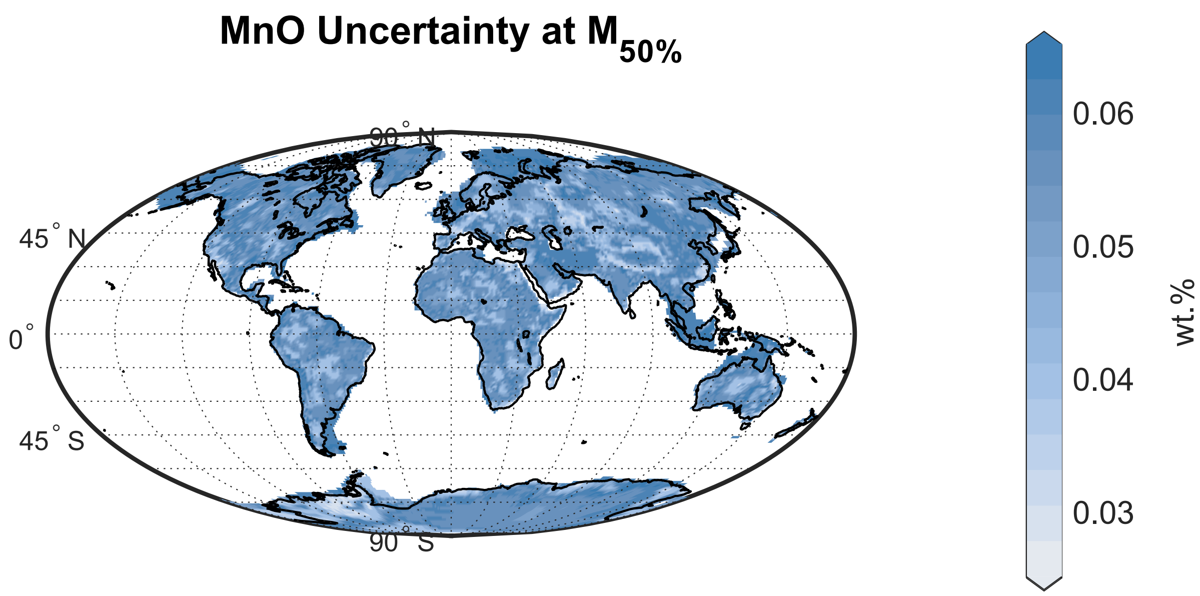
MnO Uncertainty at $M_{50\%}$
90° N
45° N
0°
45° S
90° S
0.06
0.05
0.04
0.03
wt.%

Figure S12.

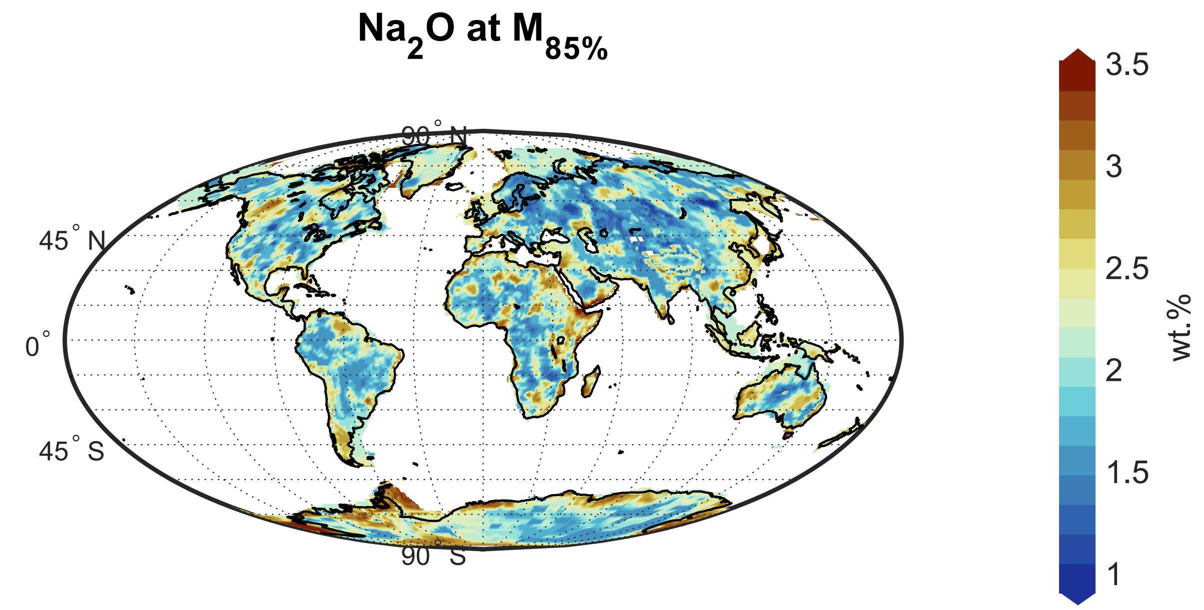
Na$_2$O at M$_{85\%}$
90° N
45° N
0°
45° S
90° S
3.5
3
2.5
2
1.5
1
wt.%

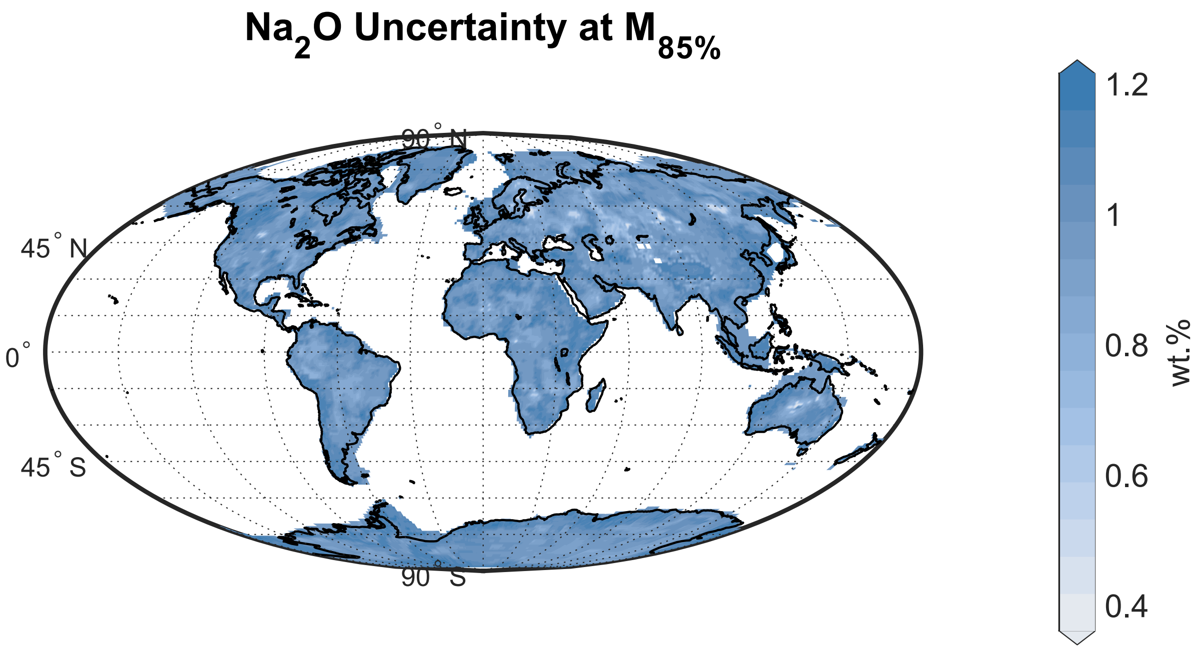
Na$_2$O Uncertainty at M$_{85\%}$
90° N
45° N
0°
45° S
90° S
1.2
1
0.8
0.6
0.4
wt.%

Figure S13.

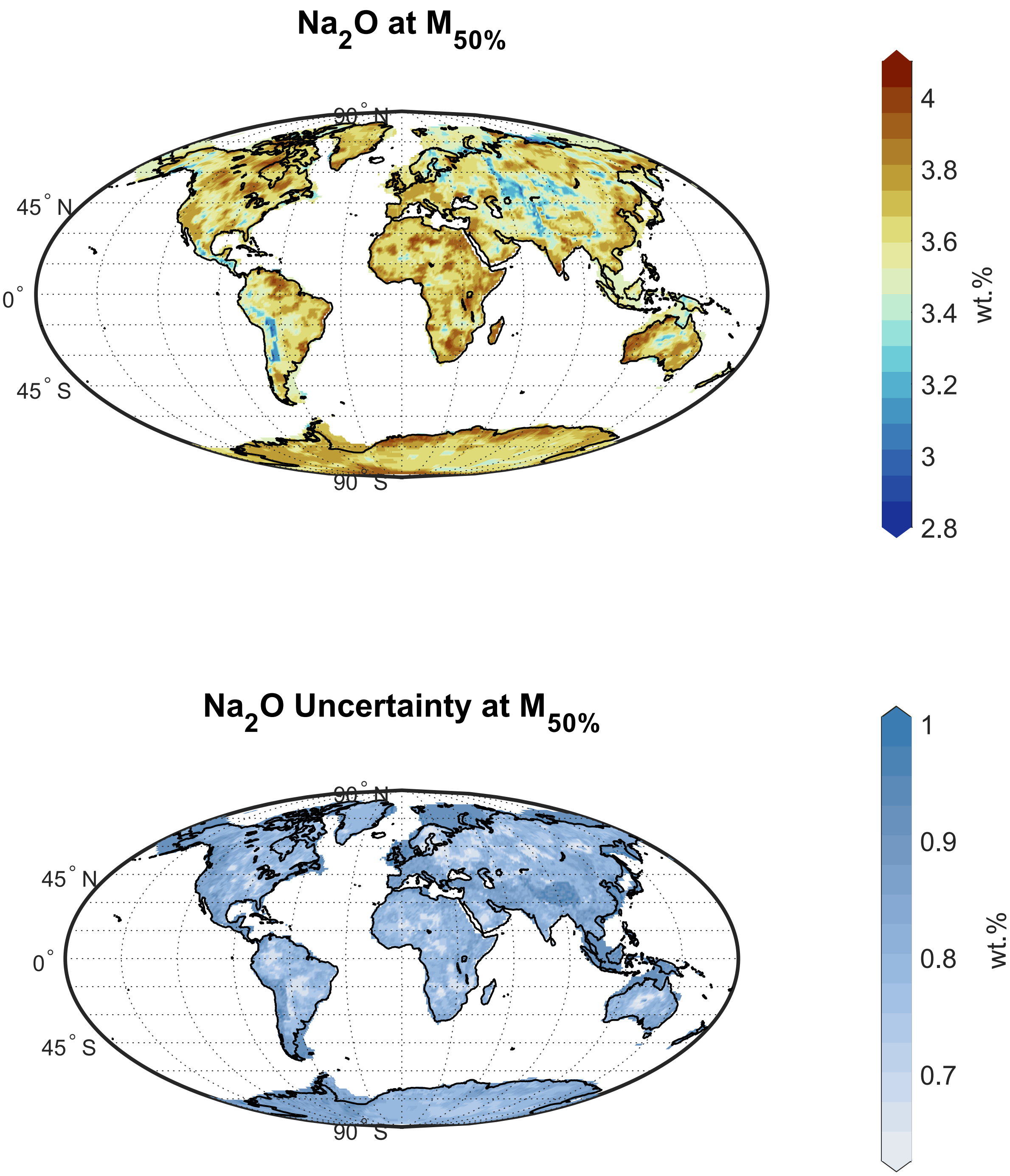
Na$_2$O at M$_{50\%}$
90° N
45° N
0°
45° S
90° S
4
3.8
3.6
3.4
3.2
3
2.8
wt.%
Na$_2$O Uncertainty at M$_{50\%}$
90° N
45° N
0°
45° S
90° S
1
0.9
0.8
0.7
wt.%

Figure S14.

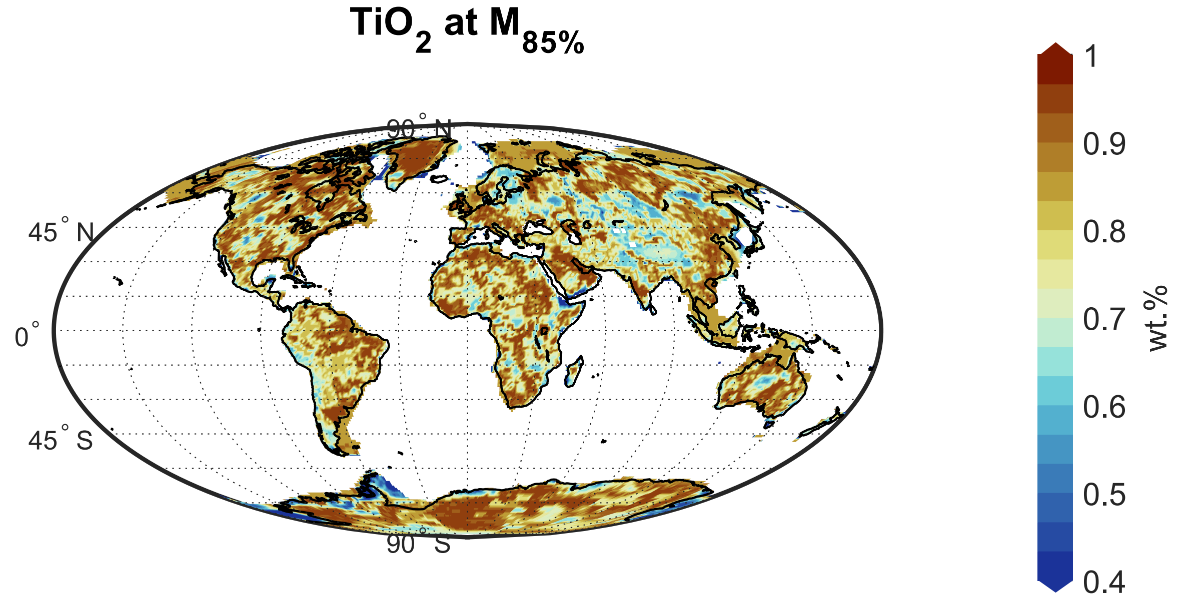
TiO2 at M85%
90° N
45° N
0°
45° S
90° S
1
0.9
0.8
0.7
0.6
0.5
0.4
wt.%

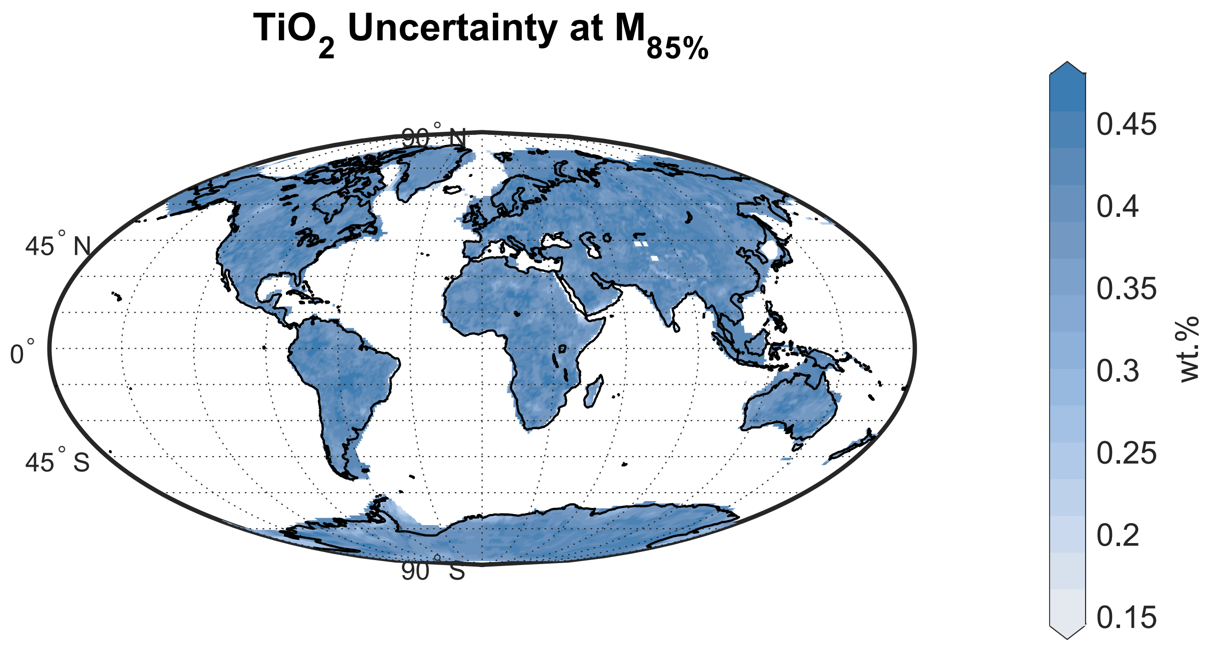
TiO2 Uncertainty at M85%
90° N
45° N
0°
45° S
90° S
0.45
0.4
0.35
0.3
0.25
0.2
0.15
wt.%

Figure S15.

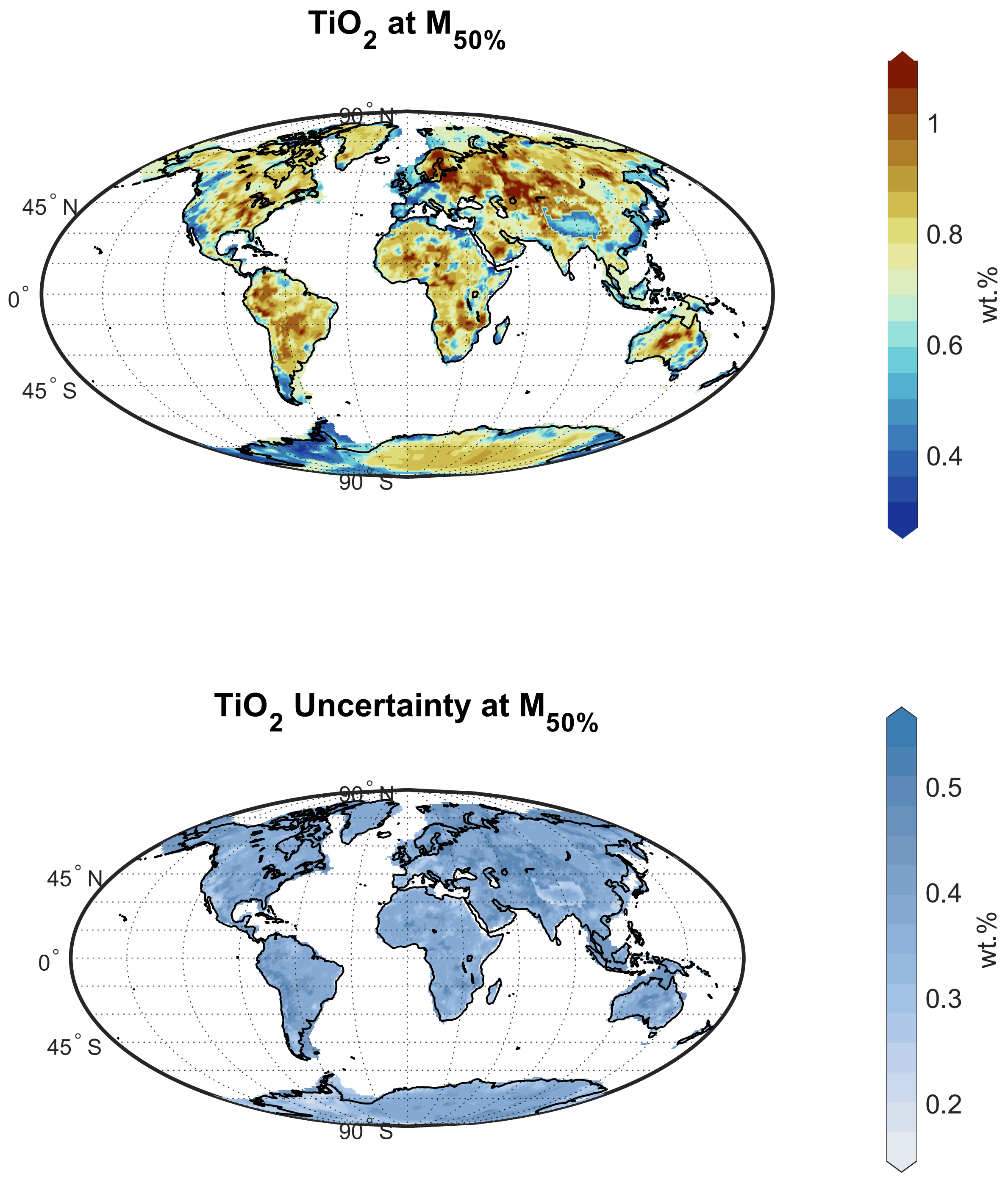
TiO2 at M50%
90° N
45° N
0°
45° S
90° S
1
0.8
0.6
0.4
wt.%
TiO2 Uncertainty at M50%
90° N
45° N
0°
45° S
90° S
0.5
0.4
0.3
0.2
wt.%

Figure S16.

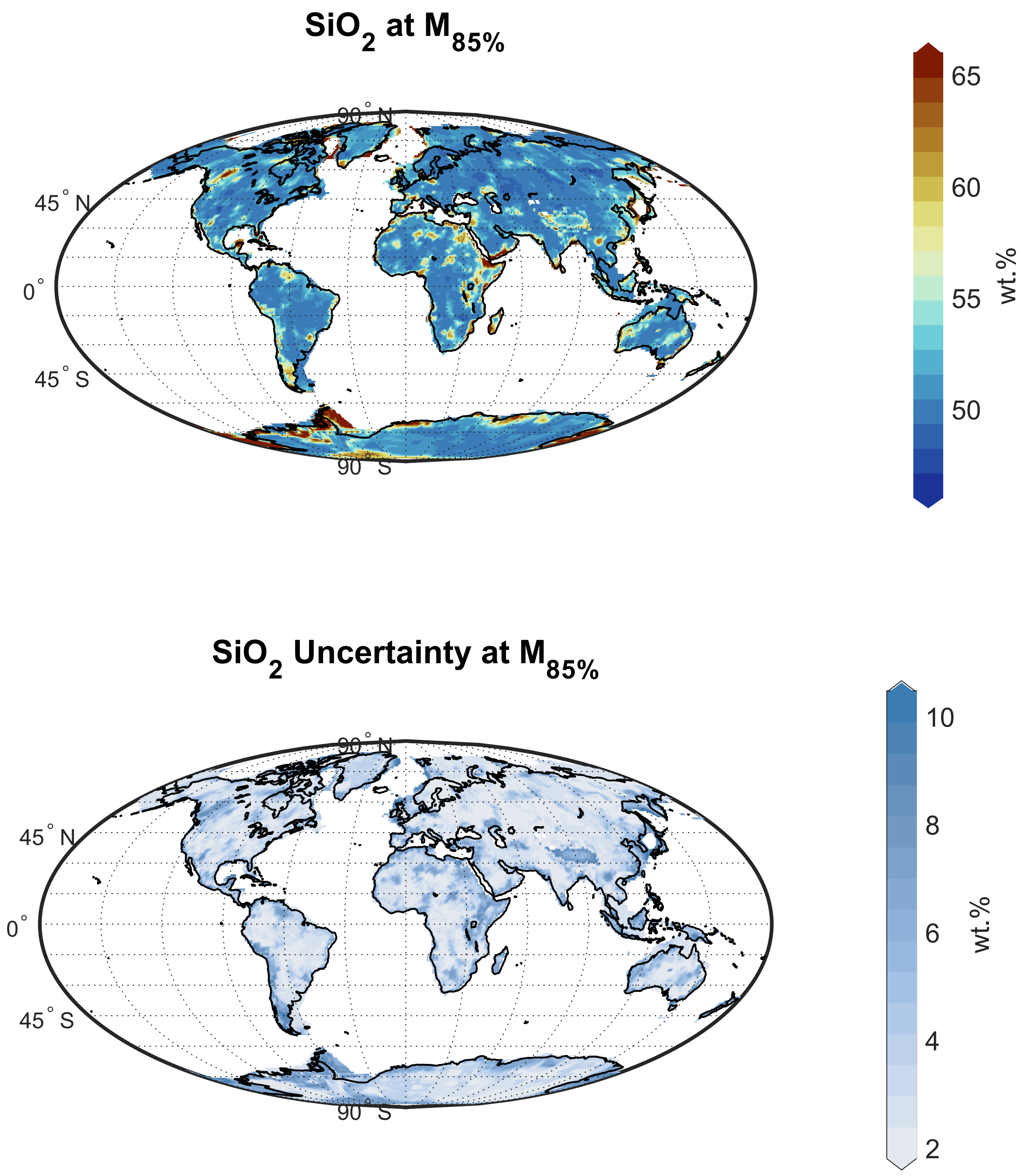
SiO_2 at $M_{85\%}$
90° N
45° N
0°
45° S
90° S
65
60
55
50
wt.%
SiO_2 Uncertainty at $M_{85\%}$
90° N
45° N
0°
45° S
90° S
10
8
6
4
2
wt.%

Figure S17.

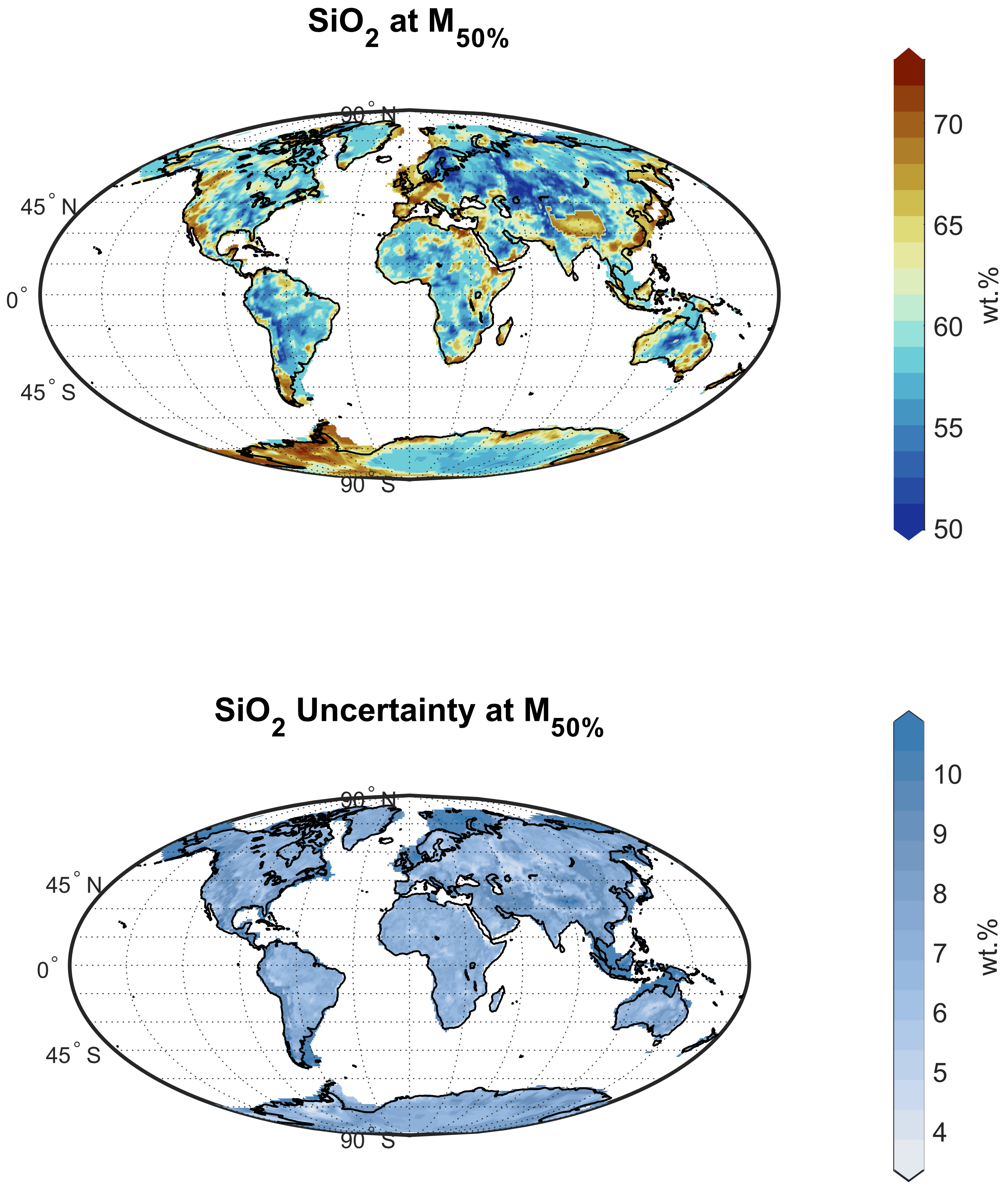
SiO2 at M50%
90° N
45° N
0°
45° S
90° S
70
65
60
55
50
wt.%
SiO2 Uncertainty at M50%
90° N
45° N
0°
45° S
90° S
10
9
8
7
6
5
4
wt.%

Figure S18.